ADVANCED MATERIALS
www.advmat.de

Visible-to-NIR Photon Harvesting: Progressive Engineering of Catalysts for Solar-Powered Environmental Purification and Fuel Production

*Min-Quan Yang, Minmin Gao, Minghui Hong, and Ghim Wei Ho**

Utilization of diffusive solar energy through photocatalytic processes for environmental purification and fuel production has long been pursued. However, efficient capture of visible–near-infrared (NIR) photons, especially for those with wavelengths longer than 600 nm, is a demanding quest in photocatalysis owing to their relatively low energy. In recent years, benefiting from the advances in photoactive material design, photocatalytic reaction system optimization, and new emerging mechanisms for long-wavelength photon activation, increasing numbers of studies on the harnessing of visible–NIR light for solar-to-chemical energy conversion have been reported. Here, the aim is to comprehensively summarize the progress in this area. The main strategies of the long-wavelength visible–NIR photon capture and the explicitly engineered material systems, i.e., narrow optical gap, photosensitizers, upconversion, and photothermal materials, are elaborated. In addition, the advances in long-wavelength light-driven photo- and photothermal-catalytic environmental remediation and fuel production are discussed. It is anticipated that this review presents the forefront achievements in visible–NIR photon capture and at the same time promotes the development of novel visible–NIR photon harnessing catalysts toward efficient solar energy utilization.

1. Introduction

The apparent incongruity between the increasing energy demand, environmental awareness, and the excessive consumption of finite fossil fuels has spurred incessant research endeavors in seeking renewable and green energy resources to maintain the sustainability of our society.[1–4] Solar energy, as an inexhaustible clean energy source that powers all the life on the Earth, is considered to be the most exploitable one.[5–7] The conversion and utilization of solar energy for chemical fuel production and environmental remediation through artificial photocatalysis has been recognized to be an ideal scheme to address the worldwide energy and environmental concerns.[8–18] Essentially, there is a need to transform the current world from a consumptive fossil fuel–powered mode into a sustainable "photons" mode.[5] To enable the large-scale application of the photocatalysis technique, improving the solar energy utilization efficiency is crucial. The sunlight covers a broad range of photon energies ranging from 250 to 2500 nm that can be divided into ultraviolet (UV), visible, and near-infrared (NIR) regions. Among which, the visible–NIR photons account for about 95% of the total solar flux that reaches the Earth surface.[19–24] Owing to their high percentage in the solar spectrum, desired artificial photocatalyst systems should be able to efficiently capture and utilize the visible–NIR photons, which essentially dominate the overall solar energy utilization efficiency.

Precedently, UV light-activated materials dominated the photocatalysis study due to the large bandgap of conventional semiconductors and their capability of exciting energetic charge carriers with high redox potentials to ignite chemical reactions.[25,26] Nonetheless, the intrinsic limitation of low ratio of UV photon in solar energy greatly hinders the ability to maximize the solar-to-chemical energy conversion efficiency.[24] In this context, developing photoactive materials with broadband light absorption characteristic has been a key task and attracted extensive research efforts in panchromatic light exploitation for photocatalysis. Empowered by the rapid advancement of nanoscience and nanotechnology, considerable progress in the catalyst design and construction is achieved. The photocatalytic materials have successfully evolved from the initial UV light response[25,27,28] to visible light excitation[29–38] as well as to the NIR light activation,[24,39,40] which substantially augments the solar energy utilization. Particularly, with the improvement in understanding the elementary photocatalysis reaction steps, a new pathway

Dr. M.-Q. Yang, Dr. M. Gao, Prof. M. Hong, Prof. G. W. Ho
Department of Electrical and Computer Engineering
National University of Singapore
4 Engineering Drive 3, 117583 Singapore, Singapore
E-mail: elehgw@nus.edu.sg
Prof. G. W. Ho
Engineering Science Programme
National University of Singapore
9 Engineering Drive 1, 117575 Singapore, Singapore
Prof. G. W. Ho
Institute of Materials Research and Engineering
A*STAR (Agency for Science, Technology and Research)
3 Research Link, 117602 Singapore, Singapore
The ORCID identification number(s) for the author(s) of this article can be found under https://doi.org/10.1002/adma.201802894.

DOI: 10.1002/adma.201802894

of harvesting visible–NIR light to induce strong solar heating, also known as photothermal effect to promote the photocatalysis process, has been proposed.[19,41,42] Notably, this strategy has a profound influence on the solar-to-chemical energy conversion and is currently the cutting-edge research for solar energy conversion field.

In view of the pivotal role of harvesting visible–NIR photon for efficient solar energy conversion and the moderate growth of researches in this topic, it is necessary to present an up-to-date review on this booming yet challenging research area. So far, a prior summary of the achievements on the solar photon harvesting is mainly focused on the extensive development conducted on UV and/or visible-light-active photocatalysts, for which the light absorption is generally in the range of 250–600 nm. The review of the successes in visible–NIR photon harvesting for photocatalysis, especially with light wavelength longer than 600 nm, is scanty. Herein, we comprehensively summarize the progress of the visible–NIR-driven photo- and photothermal-catalytic solar-to-chemical energy conversion (**Figure 1**), with an emphasis on the long-wavelength photon harvesting beyond 600 nm. The fundamental of the photocatalysis as well as the strategies of harnessing visible–NIR light is first discussed. Then, the recently engineered catalyst systems for the broad visible–NIR photon capture are covered. Accordingly, significant advances in the application of these catalysts in photo- and photothermal-catalytic H_2 production, CO_2 reduction, and in conjunction with water and air purification are highlighted. Finally, conclusions on the existing challenges along with the perspectives for further development of visible–NIR solar photon conversion through the photo- and photothermal-catalytic processes are made.

2. Fundamental of Photocatalysis and Strategies toward Visible–NIR Photon Harvesting

2.1. Fundamental of Photocatalysis

Photocatalysis mimics the nature's photosynthesis process to transform and store the sunlight energy as chemicals and fuels.[1,15] Its basic operation mechanism is that light-active materials capture photons with energy ($h\upsilon$) equal to or larger than their optical gaps to generate electron–hole pairs, in which the electrons are excited into the conduction band (CB), while the "holes" are left in the valence band (VB).[15,43] The band positions of the light-active catalysts determine the redox potentials of the generated electron–hole pairs. In a photocatalytic reaction, the bottom of CB should be more negative than the reduction potential of the reactant to be reduced (P_{red}), while the top of VB is suggested to be more positive than the oxidation potential of the reactant to be oxidized (P_{ox}). The difference between P_{red} and P_{ox} is the overall change in Gibbs free energy (ΔG) (**Figure 2**a,b).[44] When P_{red} is more anodic than P_{ox}, the ΔG is negative. Notably, the partial ΔG in the steps of reduction and oxidation by e^- and h^+ must be negative to drive a chemical reaction, which is the determining factor to trigger a photoredox process rather than the overall ΔG. Reactions with both positive and negative ΔG values can be driven by photocatalysis.[44] For example, photodegradation of organic compounds in the existence of oxygen is generally a downhill reaction (Figure 2c), while water splitting and CO_2 reduction are thermodynamic uphill reactions with large positive change in ΔG (Figure 2d).[45]

When a photocatalyst fulfills the thermodynamic requirements for a particular redox process, the reaction may take place and the rate of the reaction can be predicted by kinetics. Different kinetic models have been developed to evaluate the

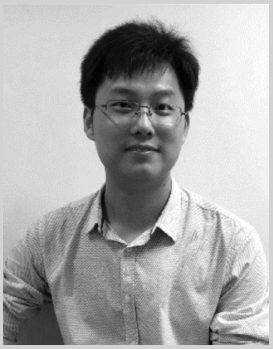

Min-Quan Yang received his Ph.D. degree in physical chemistry in 2015 from State Key Laboratory of Photocatalysis on Energy and Environment, Fuzhou University, P. R. China. He is currently a research fellow at the National University of Singapore (NUS). His research interest focuses on the synthesis of 2D materials for applications in photocatalysis and electrocatalysis.

Minmin Gao received her B.Eng. (Hons) degree in electrical engineering from National University of Singapore (NUS) in 2012, as well as her Ph.D. in 2016 under the supervision of Associate Professor Ghim Wei Ho. Her research interest currently focuses on nanomaterials for clean energy generation, photothermal water evaporation, and photocatalytic applications.

Ghim Wei Ho received her Ph.D. on semiconductor nanostructures at the Nanoscience Centre, University of Cambridge in 2006. She is an Associate Professor of the Department of Electrical and Computer Engineering at the National University of Singapore (NUS). She is also one of the pioneer associates of the Engineering Science Programme (ESP) at NUS. Her research thrust is focused on the development of functional nanostructured materials for energy, environmental and healthcare applications

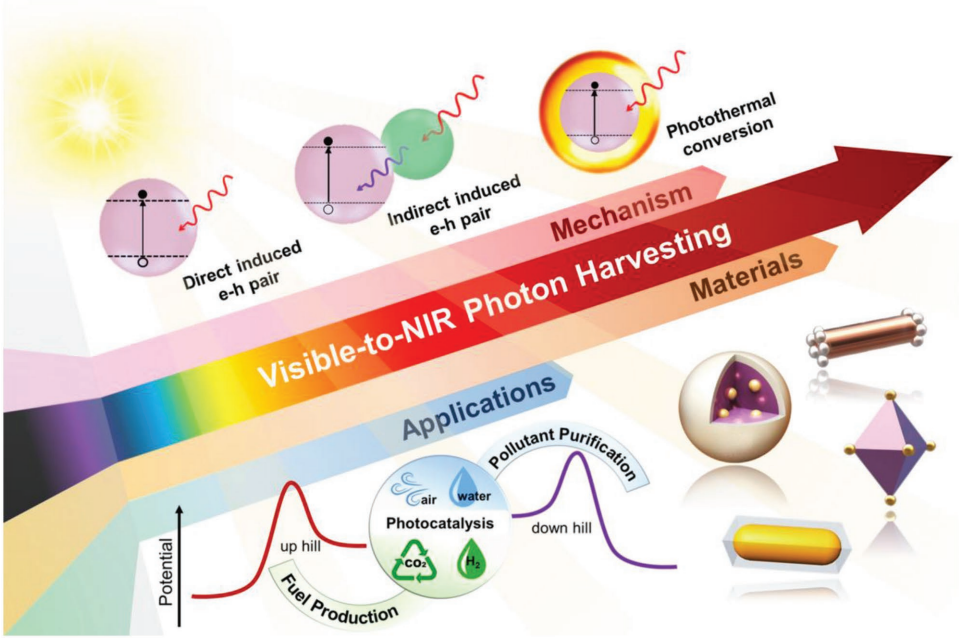

Figure 1. Overview of the contents reviewed here.

photocatalytic activity, which generally involve the formation and migration of electron–hole pairs, bulk and surface recombination of electron–hole pairs, followed by the oxidation and reduction reaction with reactants.[44] In general, after the electron–hole pairs are generated by light irradiation, the holes can either be trapped by the surface defects or to oxidize the reactant, while the electrons move randomly within the photocatalyst through a multitrapping pathway until they encounter either recombination center to recombine with holes or active center for the surface chemical reaction, thereby completing the photoredox process.[15,43,44]

2.2. Strategies toward Visible–NIR Photon Harvesting

According to the fundamental mechanism of photocatalysis, it is notable that the light absorption for generation of energetic charge carriers is the governing factor of the process. In order to improve the photocatalytic activity, enhancing solar light absorption of photocatalyst is essential. As mentioned above, most of the semiconductors used as photocatalysts have wide bandgap, which only absorb the UV region (≈5%) of the solar light, while the other ≈46% of visible light and ≈49% of NIR light[46] cannot be utilized. Extending the light absorption range of the photocatalysts to visible and NIR regions is a practical solution for adept utilization of the solar energy and thus improving the overall solar conversion efficiency. However, traditionally, it is difficult to efficiently harness the long-wavelength visible–NIR light for solar-to-chemical energy conversion due to its low photonic energy. Such low energy nature is unable to excite the typical large bandgap semiconductors and incompetent in achieving suitable redox potentials for photoinduced charge carriers. In recent years, benefiting from the advances in photoactive materials design, photocatalytic reaction system optimization, and new emerging mechanisms for long-wavelength photon activation, the difficulties faced in visible–NIR photocatalysis are successfully circumvented. Increasingly, more studies on the photocatalytic solar-to-chemical energy conversion at long visible–NIR wavelength have been reported.

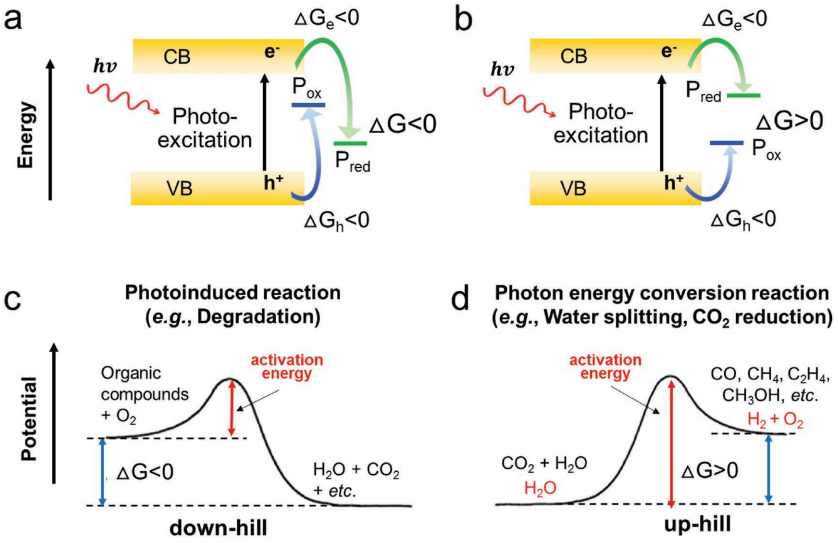

Figure 2. a,b) Electronic structure of semiconductor photocatalysts and Gibbs energy change in photocatalytic reactions. c,d) Two distinct classifications of photocatalytic reactions, namely downhill (c) and uphill (d) reactions.

Currently, the studies for long-wavelength solar energy utilization can be classified into three types based on the mechanisms of the visible–NIR photon capture, namely i) direct absorption of the long-wavelength visible–NIR photons to excite e–h pairs for triggering photoredox catalysis (direct e–h pair generation), ii) transformation of the long-wavelength visible–NIR light with low photonic energy into high energy UV–visible photons prior to e–h pairs excitation to ignite photoredox catalysis (indirect e–h pair generation), and iii) conversion of the long-wavelength visible–NIR photon energy to thermal energy for promoting photoredox catalysis (photothermal conversion). According to the three mechanisms, diverse photocatalyst systems that function under long-wavelength visible–NIR light irradiation have been developed through different strategies, including using new narrow-gap light-active materials, engineering the optical gap, decorating with photosensitizer, employing upconversion materials, and constructing photothermal systems. Among these strategies, the initial studies are mainly focused on the exploitation of new narrow-gap light-active materials and narrowing the bandgap of traditional wide-band semiconductors. Primary research revolving around this topic can be dated back to the beginning of 1980s.[47] Thereafter, employing photosensitizers was proposed as an alternative way for the absorption of long-wavelength visible–NIR light since 1985.[48] After that, the upconversion of long-wavelength visible–NIR light with low photonic energy into high energy UV–visible photons to ignite photoredox catalysis emerges. The first report was published in 2005.[49] As for the integration of solar thermal effect with photocatalyst to promote the solar energy capture, it is a new strategy proposed in the recent years. In this sense, the material evolution for the visible–NIR capture is a progressive development. Following this line, some representative examples are carefully selected and discussed in Section 3 to show the typical progress achieved in respective strategy.

3. Categories of the Visible–NIR Light Harvesters

The advanced photoactive materials reported in the literature for long-wavelength visible–NIR photon capture toward photo- and photothermal-catalytic solar fuel production and pollutant degradation have been summarized in **Table 1**. These catalysts are classified into four types, namely narrow optical gap, photosensitizer, upconversion, and photothermal materials according to the aforementioned strategies for the broad solar spectrum absorption. For these material systems, the narrow optical gap materials and photosensitizers typically adopt mechanism (i), while the upconversion and photothermal materials embrace mechanisms (ii) and (iii), respectively (**Figure 3**). The main difference for the narrow optical gap materials and photosensitizers is that the narrow-gap photocatalysts can absorb the long-wavelength visible–NIR photons to generate electron–hole pairs and drive photocatalytic reactions by themselves. Whereas for the photosensitizers, although they can also be photoexcited by long-wavelength visible–NIR photons to produce energetic charge carriers, they generally show very low or negligible photoactivity due to the fast recombination of charge carriers and lack of surface active sites. Consequently, the sensitizers are generally combined with other electron acceptors such as semiconductors to construct hybrid system for viable ignition of photoredox reactions. In the next couple of sections, typical examples of these different types of wide-spectrum visible–NIR photon harvesting materials are presented. Moreover, the limitations and possible solutions for each type of materials are discussed.

3.1. Narrow Optical Gap Materials

Developing narrow optical gap materials is thus far the most popular approach for long-wavelength visible–NIR light harnessing. Basically, two general ways are sought after: seeking new broad-light-active materials with small energy gap and narrowing the band structure of the traditional wide bandgap semiconductors. The exploration of narrow optical gap materials greatly enriches the evolution of photocatalysts. Plenty of reports are devoted to this area. In search of photoactive small bandgap materials, Huang and co-workers have reported a transition-metal hydroxide phosphate photocatalyst with broad visible–NIR absorption capability. Their pioneer work develops $Cu_2(OH)PO_4$, in which axially elongated $CuO_4(OH)_2$ octahedra share their corners with axially compressed $CuO_4(OH)$ trigonal bipyramids, as an effective NIR-responsive photocatalyst.[22] The material strongly absorbs broad solar energy with an absorption edge up to ≈2000 nm. Theoretical calculations reveal that photoelectrons are generated in $CuO_4(OH)$ trigonal bipyramids under NIR light irradiation and then transferred to $CuO_4(OH)_2$ octahedra, thus realizing an efficient electron–hole separation and enabling $Cu_2(OH)PO_4$ to be an NIR-driven photoactive catalyst. Following this work, some other theoretical calculation and experimental works about understanding the photocatalytic mechanism,[50] tuning the morphology,[51] and constructing $Cu_2(OH)PO_4$-reduced graphene oxide (rGO) hybrid composite[52] have been reported, with the aim to further improve the photocatalytic efficiency of $Cu_2(OH)PO_4$.

In addition, transition-metal sulfides are promising candidates for broad visible–NIR photon capture owing to their narrow bandgap and excellent optical absorption. Many researchers have actively studied this theme. For example, Jiang et al. have reported that Ag_2S nanoparticle is a semiconductor with a direct bandgap of 1.063 eV. It strongly absorbs in the UV, visible, and NIR regions and can be excited to generate electron–hole pairs, thus presenting excellent catalytic performance under both visible and NIR light irradiation.[53] Liu and co-workers have reported indirect WS_2 semiconductor nanosheets with a bandgap of 1.35 eV that possess broadband photocatalytic activity. The light absorption edge of the WS_2 is around 900 nm. Its VB minimum is experimentally determined to be 1.81 eV (vs NHE), and the CB is calculated around 0.42 eV, which are the befitting criteria for driving the necessary redox chemistry.[54] Additionally, $Co_{2.67}S_4$ nanoparticle with a bandgap of ≈0.92 eV has also been confirmed to exhibit optical absorption in a broad range of 240–2200 nm, encompassing the wave bands of UV, visible, and NIR regions and displaying visible to NIR light driven photocatalytic activity.[55]

Besides metal sulfides, recently, black phosphorus (BP), a newer class of 2D material, also grabs a great research attention in photocatalysis. Its tunable bandgap from ≈0.3 eV (bulk BP) to ≈2.1 eV (monolayer BP) discloses promising visible- and

Table 1. Summary of the broad visible–NIR photon harvesting photo- and photothermal catalysts with the light absorption edge greater than $\lambda > 600$ nm for solar-powered environmental purification and fuel production.

Photo/photothermal catalysts	Broadband light harvester	Light source	Wavelength for activity test	Application[k)]	Ref.
BP/WS_2[a)]	BP	[1]Xenon lamp [2]Infrared laser	[1]>780 nm [2]808 nm	P: H_2 evolution	[59]
BP/Pt/rGO	BP	[1]Xenon lamp [2]Infrared laser	[1]>780 nm [2]808 nm	P: H_2 evolution	[56]
BP/C_3N_4	BP	Xenon lamp	[1]>420 nm [2]>780 nm	P: H_2 evolution	[57]
β-$FeSi_2$	β-$FeSi_2$	N.A.[b)]	[1]>440 nm [2]>1300 nm	P: H_2 evolution	[142]
$ZnRh_2O_4$	$ZnRh_2O_4$	Xenon lamp	400 ± 10–770 ± 25 nm	P: H_2 evolution	[143]
$Ti_{12}Cr_6O_{18}(OOCC_6H_5)_{30}$	$Ti_{12}Cr_6O_{18}(OOCC_6H_5)_{30}$	Xenon lamp	[1]>400 nm [2]>800 nm	P: H_2 evolution	[23]
$CuFeSe_2$@Au nanosheets	$CuFeSe_2$	Xenon lamp	[1]>420 nm [2]>850 nm	P: O_2 evolution	[144]
WO_2–Na_xWO_3	WO_2–Na_xWO_3	[1]Xenon lamp [2]Infrared laser	[1]>420 nm [2]980 nm	P: H_2 evolution	[134]
Ag_2O/TiO_2	Ag_2O	Infrared diodes	800–1200 nm	P: H_2 evolution	[145]
V_o,N-doped In_2TiO_5	V_o,N-doped In_2TiO_5	Xenon lamp	760–1100 nm	P: H_2 evolution	[72]
Amorphous Ti^{3+}–TiO_{2-x}	Amorphous Ti^{3+}–TiO_{2-x}	Xenon lamp	[1]>420 nm [2]>750 nm	P: H_2 evolution	[70]
g-C_3N_4-Pt^{2+}	g-C_3N_4-Pt^{2+}	Xenon lamp	400–900 nm	P: H_2 evolution	[71]
WO_2–WO_3	WO_2–WO_3	Xenon lamp	400–800 nm	P: O_2 evolution	[146]
WN	WN	Xenon lamp	400–765 nm	P: overall H_2O splitting	[135]
V_o-WO_3[c)]	V_o-WO_3	Silicon nitride lamp	>800 nm	P: CO_2 evolution	[24]
V_o-BiOI	V_o-BiOI	Xenon lamp	[1]>420 nm [1]>700 nm	P: CO_2 evolution	[136]
$Cu_2(OH)PO_4$	$Cu_2(OH)PO_4$	N.A.	>800 nm	P: degradation of 2,4-dichlorophenol	[22]
$Cu_2(OH)PO_4$	$Cu_2(OH)PO_4$	Infrared lamp	>760 nm	P: degradation of 2,4-dichlorophenol	[51]
$Cu_2(OH)PO_4$/rGO	$Cu_2(OH)PO_4$	Xenon lamp	>800 nm	P: degradation of 2,4-dichlorophenol	[52]
WS_2	WS_2	[1]Mercury lamp [2]Xenon lamp [3]Infrared LED	[1]365 nm [2]>420 nm [3]855 nm	P: degradation of MO[d)]	[54]
Ag_2S	Ag_2S	Xenon lamp	>850 nm	P: degradation of MO	[53]
VS_4	VS_4	Infrared lamp	N.A.	P: degradation of MO	[147]
InSb	InSb	[1]Visible LED [2]Infrared LED	[1]400–800 nm [2]850 nm	P: degradation of MO	[148]
Ag_2O	Ag_2O	Xenon lamp	[1]>380 nm [2]>610 nm [3]>850 nm	P: degradation of MO	[149]
Cs_xWO_3	Cs_xWO_3	[1]Xenon lamp [2]Infrared lamp	[1]>400 nm [2]>800 nm	P: degradation of MB[e)]	[129]
$Co_{2.67}S_4$	$Co_{2.67}S_4$	Xenon lamp	[1]400–760 nm [2]>760 nm	P: degradation of MB	[55]
BiO_{2-x}	BiO_{2-x}	Infrared LED	770–860 nm	P: degradation of RhB and phenol[f)]	[39]
S_V-O-In_2S_3[g)]	S_V-O-In_2S_3	[1]Mercury lamp [2]Xenon lamp [3]Xenon lamp	[1]365 nm [2]>380 nm [3]>720 nm	P: degradation of MO	[150]
S_V-O-In_2S_3/TiO_2	S_V-O-In_2S_3	[1]Mercury lamp [2]Xenon lamp [3]Infrared lamp	[1]<400 nm [2]400–800 nm [3]>800 nm	P: degradation of tetracycline, MB, RhB, phenol, and salicylic acid	[151]

Table 1. Continued.

Photo/photothermal catalysts	Broadband light harvester	Light source	Wavelength for activity test	Application[k)]	Ref.
O functional-C_3N_4	O functional-C_3N_4	Xenon lamp	>800 nm	P: degradation of RhB	[152]
Ag_2O/TiO_2	Ag_2O	[1]Xenon lamp [2]Infrared LED	[1]>420 nm [2]840 nm	P: degradation of MO	[153]
Ag_2S/TiO_2	Ag_2S	[1]Mercury lamp [2] Xenon lamp [3]Infrared lamp	[1]N.A. [2]N.A. [3]N.A.	P: degradation of MO	[154]
$Ag_2O/g\text{-}C_3N_4$	Ag_2O	[1]Mercury lamp [2]Xenon lamp [3]Infrared lamp	[1]<365 nm [2]>420 nm [3]N.A.	P: degradation of MO	[155]
Ag–Ag_2O	Ag_2O	Xenon lamp	[1]>420 nm [2]>600 nm [3]>800 nm	P: degradation of 2-chlorophenol	[131]
Ag–Ag_2O	Ag_2O	[1]Mercury lamp [2]Xenon lamp [3]Infrared lamp	[1]<365 nm [2]400–780 nm [3]>780 nm	P: degradation of MO	[156]
Ag_2O/Bi_5O_7I	Ag_2O	[1]White LED [2]Infrared LED	[1]400–800 nm [3]850, 940 nm	P: degradation of bisphenol A	[157]
$Ag_2O/Ag/TiO_2$	Ag_2O	Infrared LED	880 nm	P: degradation of phenol gas	[158]
$ZnO/ZnFe_2O_4$	$ZnFe_2O_4$	[1]Mercury lamp [2]Xenon lamp [3]Infrared lamp	[1]365 nm [2]>380 nm [3]>800 nm	P: degradation of MO	[159]
H_xWO_3/WO_3	H_xWO_3/WO_3	[1]Xenon lamp [2]LED	[1]>760 nm [2]630 nm	P: degradation of MO	[160]
$rGO/Ag_2S/TiO_2$	Ag_2S	Diode laser	980 nm	P: degradation of MO	[161]
$V_o\text{-}Bi_2WO_6/TiO_2$	$V_o\text{-}Bi_2WO_6$	[1]Mercury lamp [2]Xenon lamp [3]Infrared lamp	[1]365 nm [2]>420 nm [3]>760 nm	P: degradation of MO	[21]
$W_{18}O_{49}$–TiO_2	$W_{18}O_{49}$	Infrared lamp	>780 nm	P: degradation of RhB	[162]
Cr_2O_3:P@fibrous-phosphorus	Fibrous-phosphorus	Xenon lamp	[1]400–780 nm [2]>800 nm	P: degradation of MO	[163]
Er^{3+}-doped ZnO-CuO-$ZnAl_2O_4$	Er^{3+}-doped CuO	[1]Mercury lamp [2]Xenon lamp [3]Infrared LED	[1]365 nm [2]>380 nm [3]850 nm	P: degradation of MO	[164]
$Ni_3(C_3N_3S_3)_2$	$Ni_3(C_3N_3S_3)_2$	Xenon lamp	[1]400–760 nm [2]>760 nm	P: H_2 evolution	[61]
P7-E, B-BT-1,4-E, and P17-E[h)]	P7-E, B-BT-1,4-E, and P17-E	Xenon lamp	420–700 nm	P: H_2 evolution	[62]
$Co(OH)_2$/aza-CMP[i)]	aza-CMP	Xenon lamp	[1]>420 nm [2]>800 nm	P: O_2 evolution	[165]
Zn-di-PhNcTh/$g\text{-}C_3N_4$[j)]	Zn-di-PhNcTh	Xenon lamp	420 ± 10 to 800 ± 10 nm	P: H_2 evolution	[166]
Zinc phthalocyanine/$g\text{-}C_3N_4$	Zinc phthalocyanine	Xenon lamp	420 ± 10 to 800 ± 10 nm	P: H_2 evolution	[78]
Chlorophylls/Pt/TiO_2	Chlorophylls	Xenon lamp	[1]>400 nm [2]>600 nm	P: H_2 evolution	[167]
Magnesium phthalocyanine/ Pt/g- C_3N_4	Magnesium phthalocyanine	Xenon lamp	>600 nm	P: H_2 evolution	[77]
Zinc naphthalocyanine/ TiO_2	Zinc naphthalocyanine	Xenon lamp	400–800 nm	P: H_2 evolution	[79]
Copper Phthalocyanine/Bi_2MoO_6	Copper Phthalocyanine	Red LED	620 nm	P: degradation of RhB	[168]
BP/Au nanorods/$La_2Ti_2O_7$	Au nanorods and BP	Xenon lamp	[1]>420 nm [2]>780 nm	P: H_2 evolution	[169]
Au nanorods/$La_2Ti_2O_7$	Au nanorods	Xenon lamp	[1]>420 nm [2]>780 nm	P: H_2 evolution	[170]
Au nanorods/TiO_2	Au nanorods	Xenon lamp	420–1000 nm	P: H_2 evolution	[84]
Pt-tipped Au nanorods	Au nanorods	Xenon lamp	400–1100 nm	P: H_2 evolution	[40]

Table 1. Continued.

Photo/photothermal catalysts	Broadband light harvester	Light source	Wavelength for activity test	Application[k)]	Ref.
Au nanorods/CdS	Au nanorods	Xenon lamp	[1]>570 nm	P: H_2 evolution	[81]
Au cube/cage–TiO_2–Pd cube	Au cube/cage	Xenon lamp	[1]>420 nm [2]>780 nm	P: H_2 evolution	[74]
Cu/rGO	Cu	Xenon lamp	[1]>420 nm [2]800 ± 10, 900 ± 10 nm	P: H_2 evolution	[88]
CuNi/rGO	Cu	Xenon lamp	[1]Simulate sunlight [2]800, 900 nm	P: H_2 evolution	[89]
Cu_2O/Cu	Cu	Xenon lamp	420–1000 nm	P: degradation of MO	[128]
$BiO(OH)_{0.06}Br_{0.94}$/Ag/AgBr	Ag	Xenon lamp	[1]>600 nm [2]>800 nm	P: degradation of 2-chlorophenol	[171]
Ag@P-C_3N_4/$BiVO_4$	Ag	Xenon lamp	[1]>420 nm [2]>760 nm	P: degradation of ciprofloxacin	[172]
Ag@Ag_2S	Ag	LED lamp	420, 475, 520, 655 nm	P: degradation of MO	[173]
Carbon dots-Ag/AgBr	Ag	Xenon lamp	[1]>750 nm	P: degradation of tetracycline	[174]
Au nanorods/CeO_2	Au nanorods	Diode laser	810 nm	P: degradation of acid orange 7	[85]
Au nanorods/$BiVO_4$	Au nanorods	Xenon lamp	700–800 nm	P: degradation of gaseous isopropyl alcohol	[86]
$NaYF_4$:Yb,Tm@TiO_2	$NaYF_4$:Yb,Tm	Infrared laser	980 nm	P: degradation of RhB and phenol	[96]
$NaYF_4$:Yb/Tm@TiO_2	$NaYF_4$:Yb/Tm	Infrared laser	980 nm	P: degradation of MB and crystal violet	[175]
$NaYF_4$:Yb,Tm@TiO_2	$NaYF_4$:Yb,Tm	Diode laser	980 nm	P: degradation of MB	[97]
β-$NaYF_4$:Yb,Tm@TiO_2	β-$NaYF_4$:Yb,Tm	Xenon lamp	780–2500 nm	P: degradation of RhB	[176]
$NaYF_4$:Yb,Tm@TiO_2	$NaYF_4$:Yb,Tm	Infrared laser	980 nm	P: degradation of MB	[94]
$NaYF_4$:Yb/Tm@$NaYF_4$/TiO_2	$NaYF_4$:Yb/Tm@$NaYF_4$	Infrared laser	980 nm	P: degradation of RhB	[177]
$NaYF_4$:Yb, Er,Tm@TiO_2–Ag	$NaYF_4$:Yb, Er,Tm	[1]Xenon lamp [2]Infrared diode laser	[1]>420 nm [2]980 nm	P: degradation of MO	[178]
BiOI/$ZnWO_4$:Er,Tm,Yb	Er,Tm,Yb	[1]Xenon lamp [2]Infrared laser	[1]>400 nm [2]980 nm	P: degradation of MO	[99]
Er/Tm/Yb-$CaWO_4$@(TiO_2/CaF_2)	Er/Tm/Yb	[1]High pressure mercury lamp [2]Infrared laser	[1]>780 nm [2]980 nm	P: degradation of MO	[179]
$BiVO_4$/CaF_2:Er, Tm, Yb	CaF_2:Er,Tm,Yb	Infrared laser	980 nm	P: degradation of MO	[102]
$NaYF_4$:Yb,Tm–(001)BiOCl	$NaYF_4$:Yb,Tm	Xenon lamp	>780 nm	P: degradation of MB and RhB	[98]
g-C_3N_4/$NaYF_4$:Yb,Tm	$NaYF_4$:Yb,Tm	Diode laser	980 nm	P: degradation of RhB	[180]
Er/Yb-CaF_2@TiO_2	Er/Yb-CaF_2	Xenon lamp	720–1100 nm	P: degradation of MB and MO	[181]
TiO_2@$NaGdF_4$:Yb,Tm	$NaGdF_4$:Yb,Tm	Infrared laser	980 nm	P: degradation of MB	[100]
$NaYF_4$:Yb, Er, Tm@TiO_2-Au	$NaYF_4$:Yb,Er,Tm	[1]Xenon lamp [2]Diode laser	[1]>420 nm [2]980 nm	P: degradation of MO	[104]
$NaYF_4$:Yb, Er/Au/CdS	$NaYF_4$:Yb,Er	Xenon lamp	[1]Simulate sunlight [2]>700 nm	P: H_2 evolution	[103]
$BiPO_4$:Yb,Tm/$BiVO_4$	Yb,Tm	Infrared laser	980 nm	P: degradation of MB	[182]
$NaYF_4$:Yb/Er@CdS	$NaYF_4$:Yb	Solar simulator	800–2500 nm	P: degradation of MO and carbendazim	[183]
$NaLuF_4$:Gd,Yb,Tm@SiO_2@Ag@TiO_2	$NaLuF_4$:Gd,Yb,Tm	N.A.	980 nm	P: degradation of RhB	[184]
Fe_3O_4-$NaYF_4$:Yb,Tm@TiO_2	$NaYF_4$:Yb,Tm	Xenon lamp	800–2500 nm	P: degradation of MB	[185]
Er/Tm/Yb-CaF_2/$ZnFe_2O_4$/ZnO	Er/Tm/Yb-CaF_2	High pressure mercury lamp	[1]>400 nm [2]>780 nm	P: degradation of MO and salicylic acid	[186]
$NaYF_4$:Yb,Tm@TiO_2/rGO	NaYF4:Yb,Tm	Diode laser	980 nm	P: degradation of MB, MO and phenol	[95]
Yb/Tm codoped In_2S_3	Yb/Tm	Xenon lamp	[1]420–760 nm [2]>760 nm	P: degradation of Cr(VI)	[187]
Er/Tm/Yb–($CaTiO_3$/CaF_2/TiO_2)	Er/Tm/Yb–CaF_2	High pressure mercury lamp	>780 nm	P: degradation of MO and salicylic acid	[188]

Table 1. Continued.

Photo/photothermal catalysts	Broadband light harvester	Light source	Wavelength for activity test	Application[k)]	Ref.
β-$NaYF_4$:Yb,Tm/Er@SiO_2@TiO_2	β-$NaYF_4$:Yb,Tm/Er	Infrared laser	980 nm	P: degradation of RhB	[189]
$NaGdF_4$:Er, Yb/$BiFeO_3$	$NaGdF_4$:Er,Yb	[1]Xenon lamp [2]Diode laser	[1]>420 nm [2]980 nm	P: degradation of MO and 4-chlorophenol	[190]
Yb,Er-$NaYF_4$/C-TiO_2	Yb,Er-$NaYF_4$	[1]LED [2]Infrared laser	[1]390, 455, 530, 627 nm [2]980 nm	P: degradation of NO_x	[132]
Yb,Tm-$NaYF_4$/C-TiO_2, Yb,Er-$NaYF_4$/C-TiO_2, Yb, Er-Y_2O_3/YOF/C-TiO_2	Yb,Tm-$NaYF_4$, Yb,Er-$NaYF_4$, and Yb, Er-Y_2O_3/YOF	[1]LED [2]Infrared laser	[1]390, 455, 530, 627 nm [2]980 nm	P: degradation of NO_x	[133]
$NaYF_4$:Yb,Tm/Cu_2ZnSnS_4, $NaYF_4$:Yb,Tm/$Cu_2ZnSnSe_4$	$NaYF_4$:Yb,Tm	Xenon lamp	[1]400–780 nm [2]>760 nm	P: degradation of RhB	[191]
Ag/CQDs/g-C_3N_4	CQDs	Xenon lamp	420 ± 20 to 900 ± 20 nm	P: H_2 evolution	[192]
Ag/N-GQDs/g-C_3N_4	N-GQDs	Xenon lamp	[1]>420 nm [2]>760 nm	P: degradation of tetracycline	[193]
CQDs/Bi_2MoO_6	CQDs	Xenon lamp	[1]>700 nm	P: degradation of MO	[194]
CQDs/WO_3	CQDs	Xenon lamp	>780 nm	P: degradation of RhB	[195]
CQDs/C_3N_4	CQDs	Infrared lamp	>800 nm	P: degradation of MO	[196]
CQDs/H-TiO_2	CQDs	Infrared lamp	>760 nm	P: degradation of MO	[197]
CQDs/Ag/Ag_2O	CQDs	Infrared lamp	>700 nm	P: degradation of MB and RhB	[198]
Carbon nanodots/FeOOH	Carbon nanodots	Infrared LED	740 nm	P: degradation of MO	[199]
N-GQDs/g-C_3N_4/Bi_2WO_6	N-GQDs	[1]Xenon lamp [2]Infrared lamp	[1]>420 nm [2]>700 nm	P: degradation of tetracycline	[130]
Pt/TiO_2	N.A.	Xenon lamp	Simulated solar light	PT: H_2 evolution	[200]
Ti@TiO_2	Ti	Halogen lamp	Visible–NIR light	PT: H_2 evolution	[113]
SiO_2/Ag@TiO_2	Ag	UV LED and Xenon lamp	UV–visible–NIR light	PT: H_2 evolution	[10]
CuO@TiO_2	CuO	UV LED and Xenon lamp	UV–visible–NIR light	PT: H_2 evolution	[19]
Bi/$Bi_4O_5I_2$	Bi	Xenon lamp	UV–visible–NIR light	PT: CO_2 reduction	[123]
Ag-loaded Bi_2WO_6	Ag	Xenon lamp	Simulated solar light	PT: degradation of phenol	[114]
P25–rGO	rGO	Xenon lamp	UV–visible–NIR light	PT: degradation of MB	[42]
rGO–ZnO	rGO	N.A.	UV–visible–NIR light	PT: degradation of MO	[122]
TiO_2, g-C_3N_4, BiOI ZnO, and CeO_2/Fe_3O_4@SiO_2	Fe_3O_4@SiO_2	Xenon lamp	Simulated solar light	PT: degradation of NO	[124]

[a)]BP refers to black phosphorous; [b)]N.A. refers to not available; [c)]V_o refers to oxygen vacancy rich; [d)]MO refers to methyl orange; [e)]MB refers to methylene blue; [f)]RhB refers to rhodamin B; [g)]S_V,O refers to sulfur vacancy rich and oxygen doping; [h)]P7-E, B-BT-1,4-E, and P17-E refers to three 1,4-diethynylbenzene-based linear conjugated polymers; [i)]aza-CMP refers to aza-fused conjugated microporous polymer; [j)]Zn-diPhNcTh refers to 8,9,24,25-tetra(2′,6′-diphenylphenoxy)-16(or 17)-carboxyl zinc dibenzo naphthothiophenoporphyrazine; [k)]P refers for photocatalytic application; PT refers for photothermal promoted photocatalytic application.

NIR-activated photocatalytic activity. Majima and co-workers are the first to demonstrate the potential application of BP as a visible and NIR light driven photocatalyst. They have synthesized BP nanoflakes of a few-layer thickness to construct a Pt–BP–rGO hybrid composite.[56] The BP can harness the solar photon from the UV to the NIR region to generate energetic charge carriers. With the assistance of Pt and rGO to facilitate the charge separation and consumption, the composite displays pronounced visible and NIR photoactivity.[56] Thereafter, depending on the broad and intense solar absorption characteristic of BP, especially in the visible–NIR light region, the same group has developed a series of visible–NIR photocatalyst systems such as BP–C_3N_4,[57] BP–$BiVO_4$,[58] and BP–WS_2[59] by the hybridization of BP with different semiconductors.

Apart from the traditional semiconductor materials, conjugated polymer nanostructures are emerging as new functional materials for energy conversion and storage applications. Significant attempts have been devoted to the utilization of polymers in catalysis and solar/fuel cells.[60] Explorations of conjugated polymer-based photocatalytic systems start early, but flourish only in the recent years after the report of the polymeric carbon nitride for photocatalyzing water splitting to produce H_2 under visible light.[46] The use of conjugated polymers in photocatalysis is attractive because of their low cost, facile synthesis, and excellent chemical and electrical activities. Especially, the photoelectrochemical properties of conjugated polymers can be readily tuned by varying or modifying the monomer and polycondensation method, which changes their chemical structure and geometric configurations. This effectively alters the gap and optical absorption of the polymers to a wide range of photon energy from visible to NIR light.

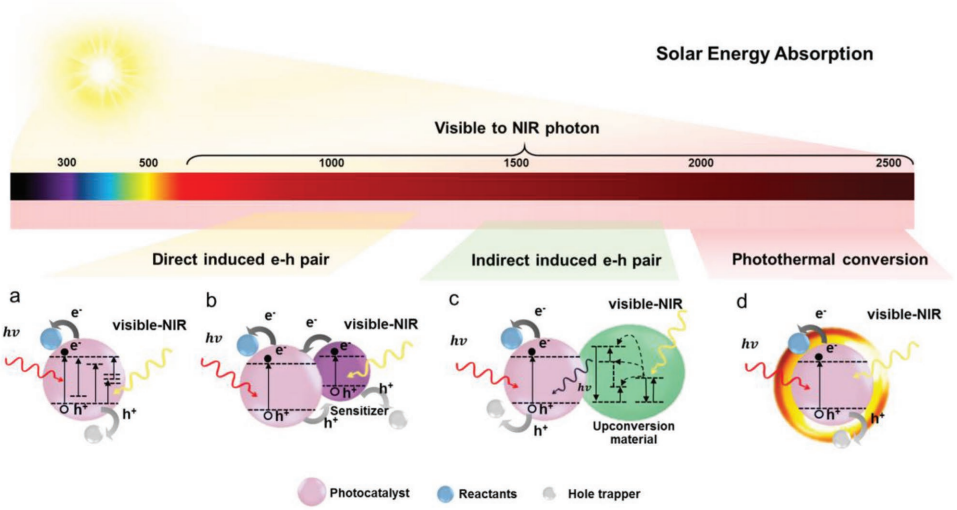

Figure 3. Strategies and corresponding material systems for broad visible–NIR photon capture: a) narrow optical gap, b) photosensitizer, c) upconversion, and d) photothermal materials.

Remita and co-workers have synthesized 1D poly(diphenylbutadiyne) (PDPB) nanostructures by direct photopolymerization of 1,4-diphenylbutadiyne (DPB) monomer (**Figure 4**a).[60] The as-prepared PDPB displays an energy gap of ≈1.81 eV. When it is illuminated by photons with energy exceeding (or equal to) the bandgap ($\lambda \leq 685$ nm), electrons and holes are formed in the conjugated polymer chains, thus promoting photoredox catalysis. Kang and co-workers have synthesized a $Ni_3(C_3N_3S_3)_2$ coordination polymer (Figure 4b) that exhibits extensive optical absorption in the UV–vis–NIR spectrum with a bandgap of about 1.31 eV (inset in Figure 4c).[61] The CB of the $Ni_3(C_3N_3S_3)_2$ is experimentally estimated to be −0.15 V versus RHE, and the VB position is calculated to be ≈1.16 V versus RHE based on its bandgap. Consequently, the as-prepared $Ni_3(C_3N_3S_3)_2$ polymer with extensive light absorption and suitable energy levels shows excellent broad spectrum–driven photocatalytic activity under UV, visible, and NIR light irradiation.

Apart from the exploration of new polymer photocatalysts, Chen and co-workers have recently reported the polymer modification stratagem to extend the light capture ability.[62] Three 1,4-diethynylbenzene-based linear conjugated polymers (namely P7-E, B-BT-1,4-E, and P17-E) are synthesized by the introduction of ethynyl group into the backbones of the

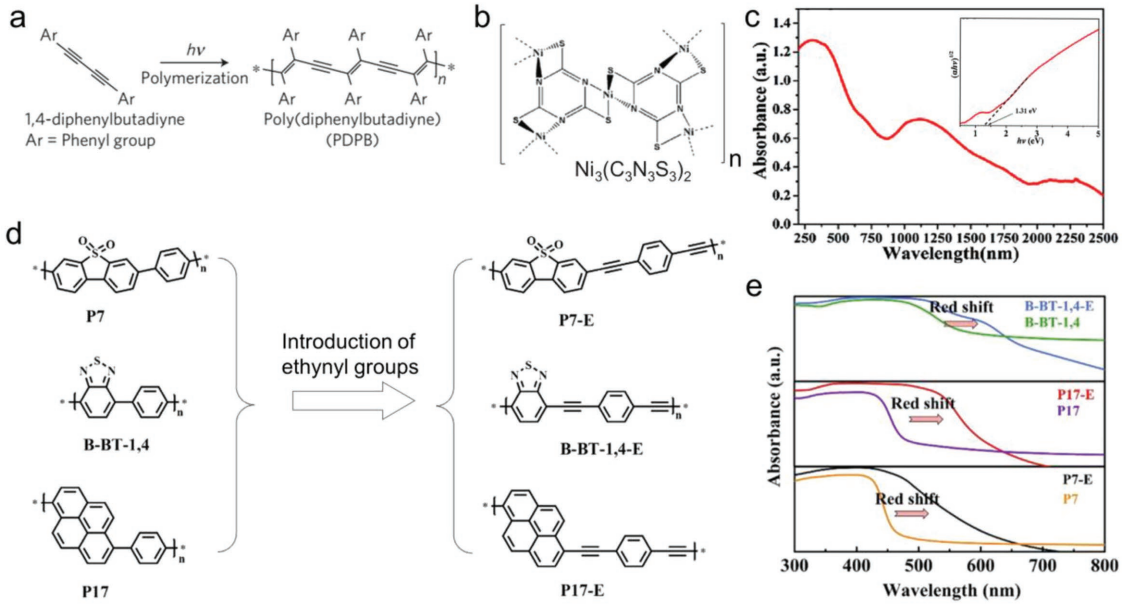

Figure 4. a) Schematic of polymerization of diphenylbutadiyne by ultraviolet irradiation. Reproduced with permission.[60] Copyright 2015, Nature Publishing Group. b) The molecular structure of $Ni_3(C_3N_3S_3)_2$ polymer; c) UV–vis–NIR diffuse reflection spectrum of $Ni_3(C_3N_3S_3)_2$; inset is the plot transformed according to the Kubelka–Munk function versus energy of light. b,c) Reproduced with permission.[61] Copyright 2017, Elsevier. d) Structures of two series of conjugated polymers; e) UV–vis diffuse reflection spectra of polymers. d,e) Reproduced with permission.[62] Copyright 2017, Elsevier.

1,4-benzene-based linear conjugated polymers of P7, B-BT-1,4, and P17 (Figure 4d). Compared with the unmodified polymers, the ethynyl group modification substantially extends the absorption edge of the P7-E, B-BT-1,4-E, and P17-E samples by 150–190 nm to the red/NIR light region (up to ≈750 nm) (Figure 4e). Importantly, negative shift of LUMO levels is also observed. The modified samples exhibit dramatically improved photoactivities compared to the unmodified ones. Especially, the B-BT-1,4-E with the broadest light absorption capability has proven to display distinct photoactivity up to 700 nm.

In addition to the exploitation of new visible–NIR light-active materials, such as semiconductors and polymers with small optical gap, the modification of traditional wide bandgap semiconductors to narrow their band energies to the visible–NIR region is another general approach. The commonly utilized method is the introduction of doping atoms, defects, and disorders, which is used to modulate electronic structure and composition stoichiometry.[63,64] In the context of material, the most actively investigated semiconductor for narrowing its bandgap is TiO_2 due to its cost effectiveness, long-term stability, and eco-friendliness traits. To date, many studies have reported diverse colored TiO_2 such as black,[65,66] green,[67] and blue[68] through various reduction methods. This has been summarized in previous reports.[69] However, most of the obtained colored TiO_2 materials fail in visible–NIR mediated photocatalysis despite their dramatically enhanced broad solar light absorption. Hence, here, we only focus on the modulated wide-bandgap semiconductors with long-wavelength visible–NIR photon capture that successfully demonstrate wide-spectrum photocatalytic activity.

In the energy band narrowing of traditional large bandgap semiconductors research scope, recently Fan and co-workers have designed a visible and NIR light sensitive amorphous Ti^{3+}-rich TiO_{2-x} (a-TiO_{2-x}) for photocatalytic application.[70] The disordered arrangement of atoms in the a-TiO_{2-x} narrows its bandgap to 1.5 eV and expands its light absorbing boundary from the UV to the NIR light region of about 1600 nm. As a result, pronounced visible–NIR light photoactivities are achieved over the as-synthesized a-TiO_{2-x} with the aid of Ti^{3+} to inhibit the charge recombination. Gong and co-workers have reported a synthesis of substoichiometric oxygen vacancy (V_o)-rich tungsten oxide (WO_{3-x}) single crystal nanosheets for broad solar light harvesting.[33] The production of copious V_o in the WO_{3-x} induces disorders at the outer surface of the nanosheets (**Figure 5**a). Optical property study of the WO_{3-x} shows that the generation of V_o engenders strong absorption in the visible–NIR region. As shown in Figure 5b, beyond the obvious optical bandgap absorption of WO_3 at 480 nm, the WO_{3-x} samples exhibit light absorption in the 480–1800 nm region. This is ascribed to a consolidated creation of discrete energy bands (480–700 nm) below the CB and the collective oscillations of surface-free CB electrons (700–1800 nm). Consequently, the incorporation of V_o to pristine WO_3 significantly enhances solar light harvesting. Moreover, Liu and co-workers have reported bandgap narrowed Bi_2WO_6 nanosheet coupled TiO_2 nanobelt heterostructure (Figure 5c) for broad solar light absorption by introduction of V_o.[21] Density functional theory (DFT) simulations show that V_o in the Bi_2WO_6 crystalline structure raises the Fermi level and reduces the band edge, facilitating interband transitions (at roughly 0.77 eV) and carrier generation under NIR illumination (Figure 5d). Consequently, the V_o-rich Bi_2WO_6/TiO_2 composite displays prominent UV to NIR photoactivities.

Additionally, Xiong and co-workers have demonstrated a concept of doping Pt^{2+} into the organic semiconductor of g-C_3N_4 (Figure 5e) to broaden its light absorption for covering an additional spectral range of 460–900 nm (Figure 5f).[71] The coordination of Pt^{2+} with the N atoms of g-C_3N_4 unit forms a metal-to-ligand charge transfer (MLCT) between them. Experimental characterizations and density of state (DOS) calculations show that the bandgap of g-C_3N_4 is 2.7 eV, while the g-C_3N_4-Pt^{2+} complex shows an upshifted LUMO state and narrowed energy gap of 1.8 eV (Figure 5g,h). Notably, the MLCT locally works in the N-conjugated aromatic units, distinctly dissimilar to the conventional HOMO–LUMO transition, hence bypasses the long-distance charge transport route that suffers from prevailing charge recombination and relaxation issues. As a result, the g-C_3N_4-Pt^{2+} exhibits enhanced photocatalytic performance under a broad-spectrum irradiation. Moreover, besides the modulation in single strategy, Hu and co-workers have established a V_o and N codoping of In_2TiO_5 (V_o,N–In_2TiO_5) with controllable bandgap for broad photon harvesting.[72] The V_o and N codoping tactic effectively moves the VB upward and induces interband energy level, leading to the bandgap reduction of the V_o,N-In_2TiO_5. As a result, NIR light irradiation can adequately excite the photoelectrons and stimulate NIR photoactivity.

In brief, exploiting narrow optical gap material is a hot topic in photocatalysis for expanding the spectral response range and improving the solar harvesting. The rapid development of material science together with the continuous research endeavor in this field greatly promotes the material evolution. Despite the progress, some challenges are also conspicuous. For effective exploitation of narrow-gap light-active materials, the band position of the photocatalyst is also an important parameter that should be considered, which determines the redox ability of the photocatalyst. The tactics of seeking new narrow bandgap material and narrowing bandgap of traditional large-bandgap photocatalysts are indeed favorable for broad light harvesting, but they adversely lower the redox potential of the photogenerated charge carriers.[73] To balance the two parameters, the fabrication of multinary band-aligned heterostructure is beneficial. The stepwise transfer and separate collection of photogenerated carriers among different photoactive components render efficient separation of charge carriers with suitable redox ability, hence enabling efficient solar energy conversion.

Moreover, for the bandgap engineering strategy, the intraband energy states produced from the doping, defect, and disorder may also function as recombination centers that result in decreased separation of charge carriers and inhibit their migration to the surface for the redox reaction. This undesirable effect is predominant when the doping, defect, and disorder concentration are high. The final photocatalytic activity is a collective outcome determined by the overall light absorption capability, charge carriers' redox ability, as well as the charge carriers' separation efficiency. Thus, a well-controlled production of doping, defect, and disorder is important to achieve a fine balance of various structural, optical, and electronic properties. In addition, theoretical calculation is a powerful tool that

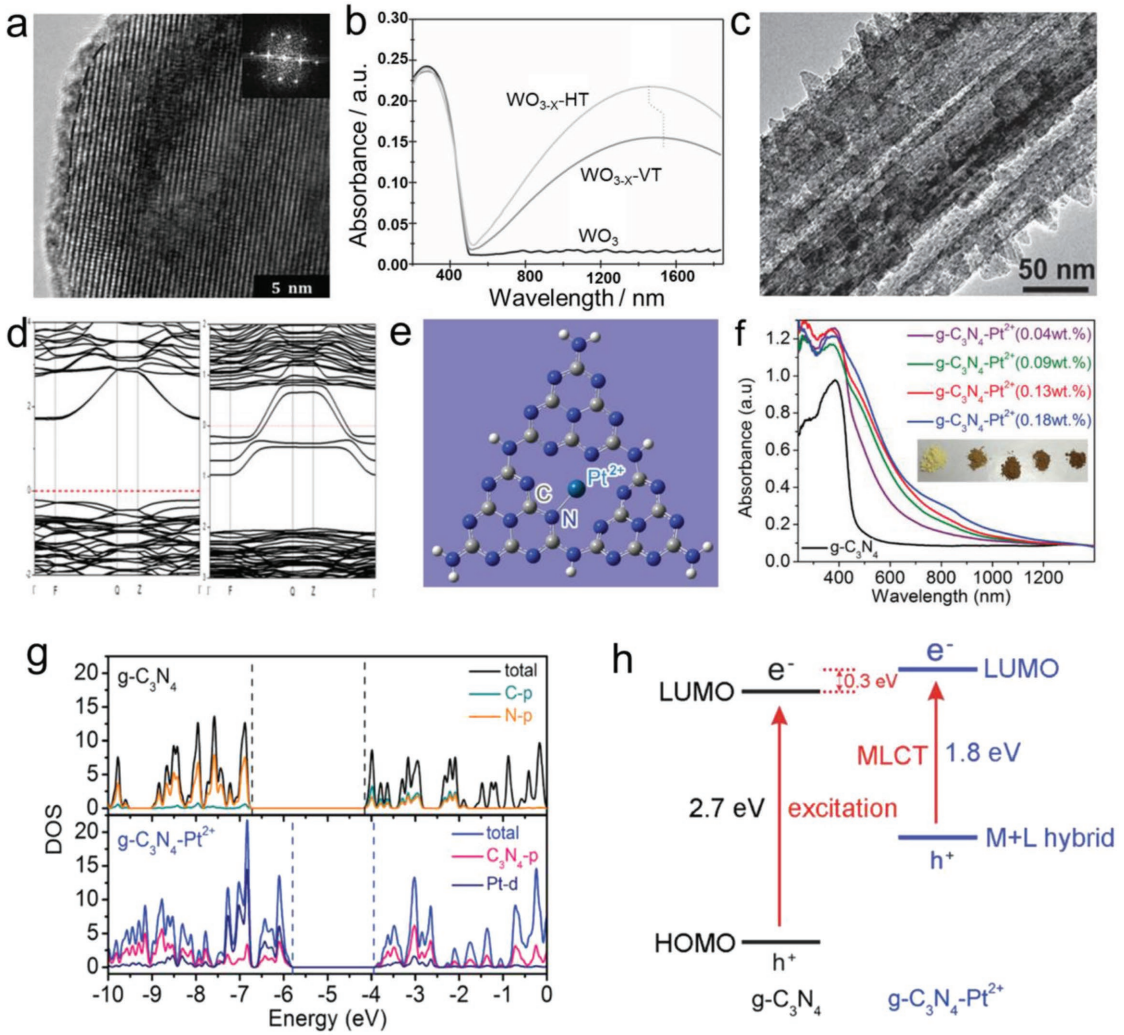

Figure 5. a) High-resolution transmission electron microscopy (HRTEM) image of the WO_{3-x}-HT nanosheets; b) UV–vis–NIR absorption spectrum of WO_3 nanosheets without and with oxygen vacancies. a,b) Reproduced with permission.[33] Copyright 2015, Wiley-VCH. c) TEM image of Bi_2WO_6/TiO_2 nanobelt heterostructure; d) band structures of pure Bi_2WO_6 (left) and Bi_2WO_6 with three O vacancies (right). c,d) Reproduced with permission.[21] Copyright 2013, Wiley-VCH. e) Structural illustration for the coordination of g-C_3N_4 with Pt^{2+}; f) UV–vis–NIR absorption spectra of g-C_3N_4 and g-C_3N_4-Pt^{2+} at various Pt concentrations; g) DOS diagrams from first-principles simulations for g-C_3N_4 and g-C_3N_4-Pt^{2+} unit cells; h) energy-band alignment diagrams for g-C_3N_4 and g-C_3N_4-Pt^{2+} as revealed in panel (g). e–g) Reproduced with permission.[71] Copyright 2016, Wiley-VCH.

aids the fundamental understanding of the electronic band modulation. A joint effort between experiment and theory will lead to the targeted design of broad light responsive photocatalyst for attaining ideal catalytic performance.

3.2. Photosensitizers

Photosensitizer decoration is another method for direct utilization of the long-wavelength visible–NIR photon to generate charge carriers. This method involves activating a visible–NIR light responsive material (sensitizer) to generate electrons, which are then injected into the electron acceptor for the surface redox reaction. Dyes and surface plasmon resonance (SPR) materials are two main groups of sensitizers extensively studied in artificial photocatalysis. The light absorption of dye is strongly correlated to the type and molecular structure, while the resonant light wavelength and intensity of SPR material depend on the morphology (i.e., shape and size) and surrounding environment. The modifiable molecular structure of the dye and the tunable SPR nanostructure support the photosensitization effect to cover a broad range of the visible–NIR photon spectrum, which is crucial for promoting the solar energy capture.

Moreover, in the photosensitization scheme, the electrons transfer from the sensitizer to the electron acceptor (generally the CB of semiconductor) can maintain relatively high-energy states, as determined by the CB characteristic of semiconductor.[74] As such, this scheme enables the utilization of the low-energy visible–NIR photons while providing sufficiently high redox ability for surface reactions, which cannot be achieved by a bare semiconductor system. Furthermore, the

photosensitization system holds another niche in suppressing the recombination of electron–hole pairs depending on the interfacial energy gap between the photosensitizer donor and the semiconductor acceptor, which inhibits the backflow of photoelectrons to the sensitizer and favorably facilitates the spatial separation of charge carriers.[74]

In the dye photosensitization, electron–hole pairs are generated upon highest occupied molecular orbital to lowest unoccupied molecular orbital (HOMO–LUMO) excitation. The electrons are transferred to the electron acceptor, while the holes react with the electrolyte to regenerate the dye and sustain the photocatalytic reaction.[14,75,76] For efficient electron transport, the intimate interfacial contact between the dye and the surface of photocatalyst is important.[75,76] Conventionally, Ru-complex dyes, metalloporphyrins, and plentiful organic dyes, such as the eosin Y, erythrosine, rose bengal, fluorescein, and rhodamine 6G, are the most widely studied sensitizers for solar energy capture.[75,76] However, these classical dyes generally absorb in the region of 400–600 nm with maximal absorption peaks at ≈490–560 nm, which is insufficient for the visible–NIR light harnessing. In the past years, the breakthrough in nanomaterials synthesis leads to the development of some novel dye photosensitizers with wider light absorption at wavelength longer than 600 nm.

For example, phthalocyanines (Pcs) are chromophores well known for their intense absorption in the red/near-IR spectral regions (650–800 nm) and excellent chemical/thermal stability as well as appropriate redox property, which render them attractive candidates for the dye-sensitized wide visible–NIR light capture. Domen and co-workers have investigated the sensitization of a mesoporous g-C_3N_4 photocatalys by depositing magnesium phthalocyanine (MgPc, **Figure 6**a) on its surface,[77] which results in distinct visible–NIR photon absorption (Figure 6b). The as-synthesized sample shows stable photocatalytic activity under the irradiation at wavelength longer than 600 nm, which greatly surpasses the absorption edge of the principal g-C_3N_4. Similarly, Peng and co-workers have reported the utilization of highly asymmetric zinc phthalocyanine derivative (Zn-tri-PcNc, Figure 6c) with intense near-IR light (650–800 nm) absorption as a sensitizer to extend the spectral response of g-C_3N_4.[78] The hybrid Zn-tri-PcNc/g-C_3N_4 exhibits broad absorption band across the visible–NIR light region (Figure 6d), whereas the pristine g-C_3N_4 only shows an absorption onset at ≈450 nm. Notably, the Zn-tri-PcNc/g-C_3N_4 yields considerable photoactivities in the visible–NIR light region beyond 700 nm.

Besides the phthalocyanines, squaraine dyes are other types of sensitizers that respond to visible–NIR light ranging from 500 to 900 nm, which have also been utilized in photocatalytic visible–NIR energy conversion. Peng and co-workers have reported the zinc naphthalocyanine (Zn-tetra-Nc) (Figure 6f) and Zn-tri-PcNc sensitizers for expanding the spectral response of TiO_2 semiconductor.[79] The composites of Zn-tri-PcNc/TiO_2 and Zn-tetra-Nc/TiO_2 show broad light absorption from ≈550 to 900 nm (Figure 6e). Obvious fluorescence quenching effects are observed when Pt/TiO_2 is added to the above dye solutions

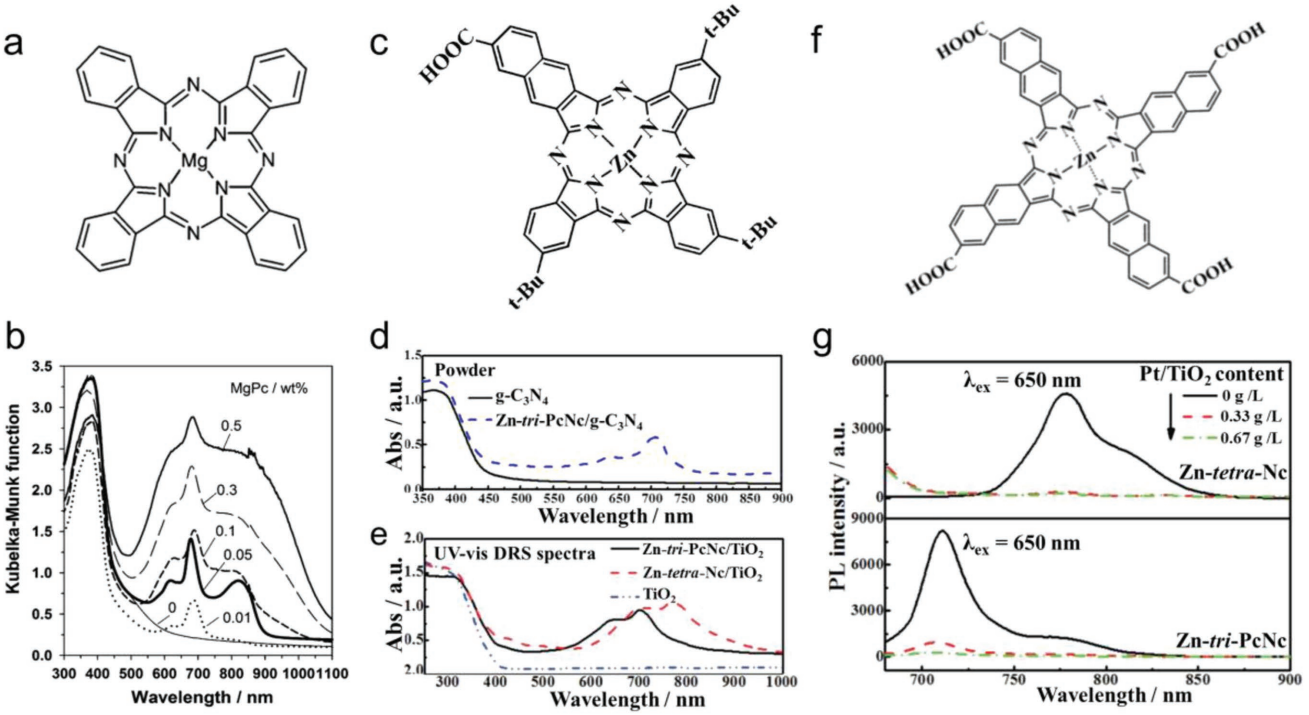

Figure 6. a) Molecular structure of magnesium phthalocyanine (MgPc); b) UV–vis–NIR diffuse reflectance spectra of g-C_3N_4 modified with various amounts of MgPc. a,b) Reproduced with permission.[77] Copyright 2010, Royal Society of Chemistry. c) Molecular structure of zinc phthalocyanine derivative (Zn-tri-PcNc); d) UV–vis–NIR diffuse reflectance absorption spectra of g-C_3N_4 and Zn-tri-PcNc/ g-C_3N_4. c,d) Reproduced with permission.[78] Copyright 2014, American Chemical Society. e) UV–vis–NIR diffuse reflectance absorption spectra of TiO_2, Zn-tri-PcNc/TiO_2, and Zn-tetra-Nc/TiO_2; f) molecular structure of zinc naphthalocyanine (Zn-tetra-Nc); g) photoluminescence spectra of the Zn-tri-PcNc and Zn-tetra-Nc solutions (10×10^{-6} M) with different Pt/TiO_2 contents. e–g) Reproduced with permission.[79] Copyright 2013, Royal Society of Chemistry.

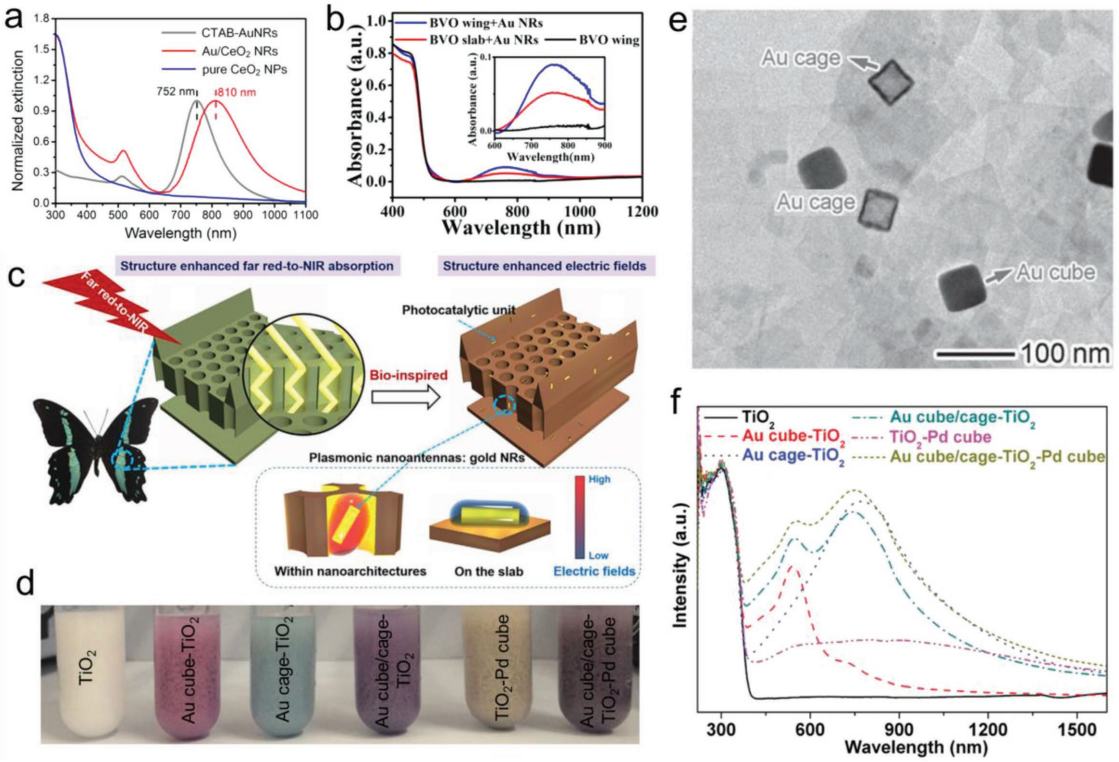

Figure 7. a) Normalized extinction spectra of the Au NRs, Au/CeO_2 NRs, and pure CeO_2 nanoparticles. Reproduced with permission.[85] Copyright 2016, American Chemical Society. b) Experimental optical absorption of Au NR-loaded $BiVO_4$ wing; the inset shows the amplification from 600 to 900 nm in (b); c) schematic illustration of the concept of structure-enhanced bioinspired far red-to-NIR highly responsive photocatalytic system. b,c) Reproduced with permission.[86] Copyright 2016, Nature Publishing Group. d) Photograph of suspensions; e) TEM image of Au cube/cage–TiO_2 hybrid structure; f) UV–vis–NIR diffuse reflectance spectra of different samples. d–f) Reproduced with permission.[74] Copyright 2016, Wiley-VCH.

(Figure 6g), indicating that the charge carriers generated from the photosensitization of Zn-tetra-Nc and Zn-tri-PcNc can efficiently be separated and transferred to the TiO_2, thus endowing Zn-tri-PcNc/TiO_2 and Zn-tetra-Nc/TiO_2 with visible–NIR photoactivities.

Dye aside, plasmonic metal is another group of material that can be used as photosensitizer. The SPR effect refers to the photoinduced coherent oscillation of surface conduction electrons and is generally characterized by strong light absorption and/or scattering in particular regions.[80–82] The exact position and shape of the SPR band depend on many factors, including particle size, shape of the material, dielectric constant of the medium, and Coulombic charge among the nanoparticles.[41] In the SPR excitation process, when the incident photon frequency matches the frequency of electrons oscillating against the restoring force of positive nuclei, the plasmonic materials can be excited and several processes can be induced: i) near-field optical enhancement, ii) hot electron–hole transfer, and iii) localized plasmonic heating effect.[83] The first two mechanisms will contribute to the photogeneration of electron–hole pairs, while the localized plasmonic heating is a photothermal effect that can promote the photocatalytic activity and is discussed later.

In the SPR sensitization, metallic Au, Ag, and Cu nanostructures are the most widely demonstrated plasmonic materials to display extraordinary SPR effect under light irradiation. In general, these metals with nanoparticle structure show typical photoabsorption in the visible light region below 600 nm,[84] which is insufficient for capturing longer wavelength NIR photon. In recent years, by precise engineering of the size, shape, and surrounding media of the plasmonic metal nanostructures, the SPR-induced light absorption has been markedly extended to the NIR region, which plays a pivotal role in the long-wavelength visible–NIR photons harvesting.

For instance, Au nanorods (Au NRs) with different aspect ratio display tunable SPR absorption ranging from visible to NIR regions (600–1200 nm).[84] Their integration with efficient electron acceptor to construct Au NR-based plasmon photocatalysts for enhancing the solar energy utilization has been reported by different groups. Zhou and co-workers have prepared a well-defined CeO_2-coated Au NR composite.[85] The as-prepared Au/CeO_2 core/shell structure displays characteristic plasmon absorption band of Au in the NIR region (**Figure 7**a). Notably, in comparison with the bare Au nanorods, the coating of CeO_2 redshifts the SPR band from 752 to 810 nm, pertaining to the change of the dielectric environment around the plasmonic particles. The resulted Au/CeO_2 core/shell nanostructure evidently establishes plasmon-enhanced NIR photocatalytic activities. Fan and co-workers have reported a bioinspired $BiVO_4$ wing–Au NR photocatalyst system by controlled assembly of light-harvesting plasmonic Au antenna onto the 3D micro/nanoarchitectures of $BiVO_4$ photocatalytic unit synthesized from butterfly wing template (Figure 7c).[86] The composite presents light absorption at 600–900 nm, as shown in Figure 7b. Notably, the absorption

peak of the $BiVO_4$ wing–Au NRs reaches almost twice that of nonstructured counterpart, which has been associated with the unique electric-field amplitude of SPR of the $BiVO_4$ wings' 3D architecture. This SPR enhancement promotes the rate of visible–NIR light-induced electron–hole pair formation and substantially reinforces the $BiVO_4$ wing–Au nanorod with far-red to NIR light photoactivities. Moreover, in addition to the nanorod structure, in a recent work of Xiong and co-workers, Au nanocubes and Au nanocages have been integrated to TiO_2 (Figure 7e) nanosheets for achieving broad-spectrum light utilization.[74] The color of the hybrid samples changes dramatically with the incorporation of Au nanocages or/and nanocubes onto TiO_2 (Figure 7d). UV–vis–NIR diffuse reflectance spectra show that the Au nanocubes capture light in the visible region of ≈400–600, while the Au nanocages exhibit a plasmonic band in the range of 600–1000 nm (Figure 7f). The combinative utilization of Au nanocubes and nanocages endows the Au–TiO_2 composite with conspicuous photoactivity under both visible and NIR light irradiation.

Besides Au nanostructures, Ag and Cu nanometals with long-wavelength visible–NIR photon capture have also been designed for broad-spectrum photocatalysis. Hsu and co-workers have fabricated Ag nanoparticle-decorated SiO_2 nanospheres that display appreciable photocatalytic activities upon SPR excitation.[87] The composites show Ag size-dependent SPR absorption. A significant redshifting and broadening of SPR peak is observed with the reduction of Ag particle size. This can be explained by the electromagnetic coupling effect between individual metal nanoparticles. When the Ag nanoparticles with reduced dimension come in close proximity, they will enhance the polarizability of the electron cloud to lower the plasmon resonance energy and result in the redshift of SPR. The Ag–SiO_2 sample with the smallest Ag size ensues the broadest visible–NIR band absorption that manifests in the highest photoactivity. Additionally, in recent works of Zeng and co-workers, they have constructed two Cu-based visible–NIR photocatalysts of Cu nanoparticle–rGO nanosheets[88] and dendrite-like plasmonic CuNi bimetal–rGO composite[89] based on the SPR absorption of Cu. In the composites, light-induced electron–hole pairs are generated from the SPR effect of Cu. Importantly, owing to the broad-spectrum response of plasmonic Cu, NIR photocatalytic activities are confirmed for the Cu–rGO and CuNi–rGO systems with monochromatic light irradiation.

Furthermore, aside from these well-studied Au, Ag, and Cu nanostructures that have distinct visible–NIR absorption peaks, noble metal Pt is also proven to be a promising broad-spectrum light harvester for improving the photoactivity of semiconductor. Xu and co-workers have reported the observation of localized visible light absorption of small Pt nanoparticles (<10 nm) in Pt/SiO_2@TiO_2 composite and the rational tuning of the absorption peak to long wavelength by adjusting the dielectric environment of Pt nanoparticles instead of changing their size.[38] In the design, Pt particles with dimensions of 2–5 nm are controllably distributed on the SiO_2 support via an electrostatic self-assembly method, followed by a fine-coating of thin TiO_2 layer to form a core–shell structure. The self-assembled Pt/SiO_2-SA empowers the supported Pt nanoparticles to absorb the scattered light in the near field of the dielectric surface of SiO_2, which thus exhibits distinctly enhanced visible light absorption peaks correlated to the scattering resonances of the SiO_2 support (**Figure 8**a). An increase in SiO_2 diameter can lead to an obvious redshift of the scattering and absorption peaks of Pt/SiO_2-SA. Moreover, with the coating of a thin TiO_2 layer, the light absorption position, intensity, and profile of the Pt nanoparticles vary with their loading weight (Figure 8b). This can be ascribed to the change in the dielectric environment of the Pt nanoparticles induced by the TiO_2 semiconductor shell. Eventually, as a result of the excitation of Pt nanoparticles by absorbing scattered light, hot electrons can be generated in the Pt/SiO_2@TiO_2 core–shell configuration, which can transfer to the CB of the TiO_2 across the intimate interfacial contact to drive surface reduction reactions (Figure 8c). Meanwhile, photogenerated holes move to the surface of the TiO_2 shell by "tunneling effect" to react with an electron donor due to the thinness of the TiO_2 coating, less than 10 nm. Controlled wavelength-dependent experiments show that the Pt/SiO_2@TiO_2 composite displays obvious photoactivity under visible light irradiation with the wavelength up to 650 nm, providing robust evidence for the broad-spectrum harvesting and the improved solar energy conversion efficiency.

In general, the utilization of photosensitizers with tunable photoabsorption offers new opportunities to extend the light absorption of photocatalytic systems to longer wavelength, while imparting sufficiently high redox ability of photogenerated charge carriers to garner visible–NIR photoactivity. Nevertheless, the photosensitization-induced solar-to-chemical energy conversion efficiency is still lower than the traditional semiconductor-driven photocatalysis. One of the major restrictions for the low solar conversion efficiency is the limited light absorption of the single photosensitizer. Most of the dye and SPR materials can only absorb the visible–NIR light in a range of dozens to hundreds of nanometers with a maximum absorption peak, while failing to harness the remaining fraction of the solar spectrum. In principle, three solutions are proposed to solve the limitation. The first one is to tailor the morphology, structure, and composition (e.g., fabrication of nanocages, nanorods and nanoplates, and construction of alloy metals) of plasmonic metals, as well as tuning the composition of dyes, by which the light absorption range can be extended. Many current studies are focused on this strategy. Another way is to integrate multiple plasmonic sensitizers and dyes with different yet complementary light absorption ranges into one hybrid system, which is similar to the fabrication of heterostructured semiconductor systems. This is an easier and more accessible way for realizing broad visible–NIR light harvesting. The last strategy is to exploit new photosensitizers. For instance, recent studies have shown that Au clusters with a size regime of 1–3 nm can generate electron–hole pairs upon HOMO–LUMO transition induced from the ligand-to-metal charge transfer,[90] which displays light absorption character like that of semiconductor and can perform as visible light photosensitizer. Although the light absorption range of the Au clusters necessitates further extending, their sensitization efficiency has proven to be higher than Au plasmonic metals.[90] This would be an alternative way for promoting the photocatalytic solar energy conversion.

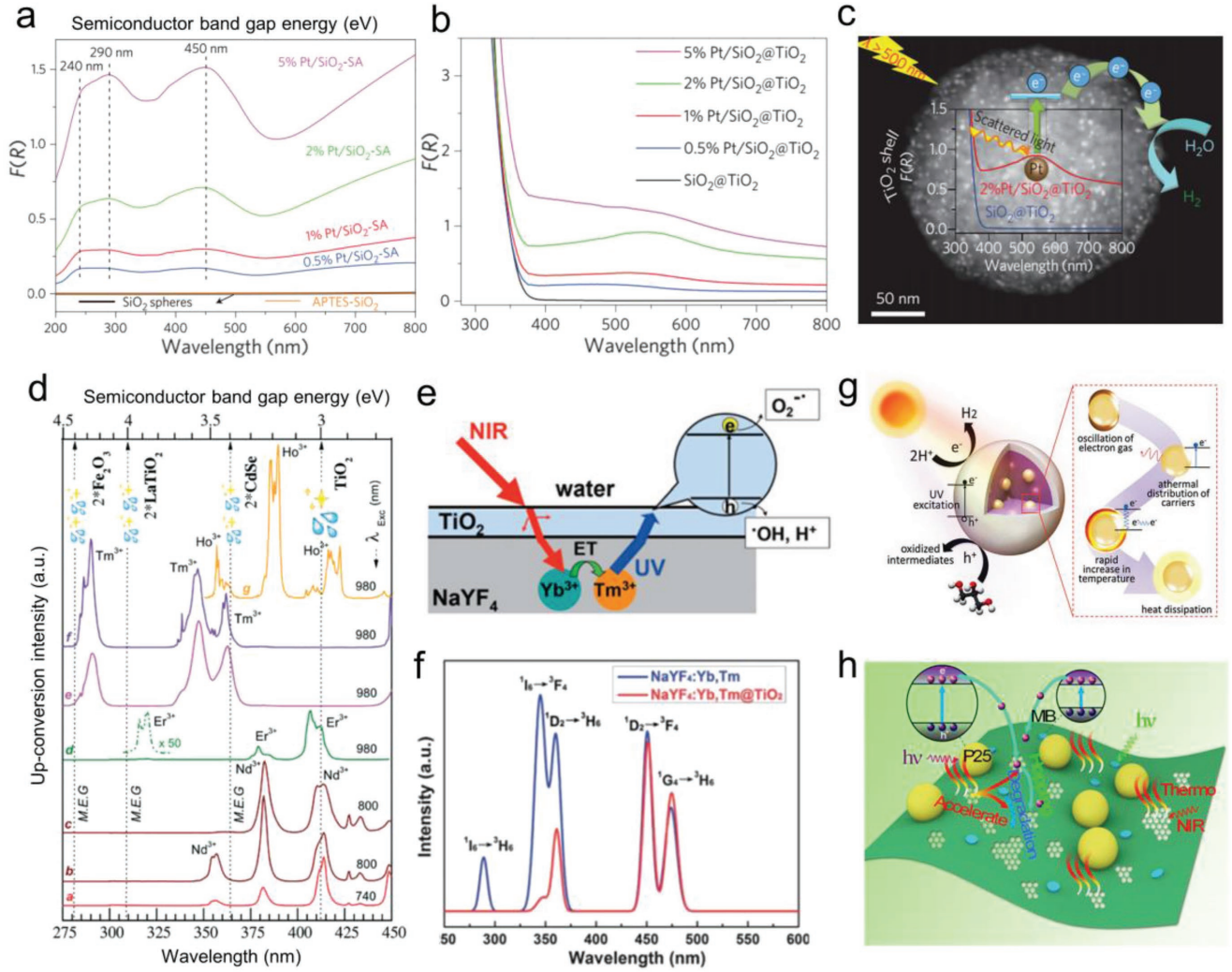

Figure 8. a) UV–vis diffuse reflectance spectra of SiO_2 spheres, 3-aminopropyltriethoxysilane (APTES)–SiO_2, and the supported Pt/SiO_2-SA composites with different weight contents of Pt plotted as the Kubelka–Munk function of the reflectance R; b) UV–vis diffuse reflectance spectra of SiO_2@TiO_2 and Pt/SiO_2@TiO_2 composites with different weight contents of Pt; c) schematic illustration of charge transfer in the Pt/SiO_2@TiO_2 composites under visible light. a–c) Reproduced with permission.[38] Copyright 2016, Nature Publishing Group. d) Upconversion spectra in the UV–blue region of Ln doped oxyfluoride nanoglass-ceramics comprising: a–c) PbF_2, d) $NaYF_4$, e) YF_3, and f,g) KYF_4 nanocrystals, under red and near-infrared excitation. Reproduced with permission.[141] Copyright 2013, Elsevier. e) The upconversion based photocatalysis process over $NaYF_4$:Yb,Tm@TiO_2 composite; f) upconversion PL spectra of the $NaYF_4$:Yb,Tm microrods and $NaYF_4$:Yb,Tm@TiO_2 composite. e,f) Reproduced with permission.[94] Copyright 2013, Royal Society of Chemistry. g) Schematic diagram of the proposed mechanism of photothermic water splitting with Ag. Reproduced with permission.[10] Copyright 2016, Royal Society of Chemistry. h) Photothermal MB degradation with graphene–TiO_2. Reproduced with permission.[42] Copyright 2014, American Chemical Society.

In addition, the sluggish photoelectron transfer from the sensitizer to the electron acceptor is another bottleneck for the low photosensitization efficiency. The rapid electron–hole recombination or electron–electron scattering process of the excited sensitizer intensely competes with the interfacial electron transfer. High-performance photosensitization requires fast and efficient interfacial charge separation. In this regard, the fixation of photosensitizer, particularly for dye molecule, on electron acceptor by introducing a linker stronger than common physical adsorption is a feasible way. In addition, the surface modification is essential for both dye and plasmonic metal in facilitating charge separation and surface reaction kinetics. Furthermore, for the SPR metal, the rational construction of nanosystem architecture such as metal core–semiconductor shell and metal tip–semiconductor rod is of great significance for promoting the interfacial charge transfer, which can markedly improve the sensitization efficiency and thus the solar utilization efficiency.

3.3. Upconversion Materials

Photon upconversion is an anti-Stokes emission process in which the sequential absorption of two or more photons leads to the emission of light at a shorter wavelength than the excitation wavelength.[91–93] The phenomenon has been known since 1960s,[91] but has been primarily exploited for the development of some remarkably effective optical devices such as infrared

quantum counter detectors. In photocatalysis, the upconversion process is a key strategy for capturing the long-wavelength visible–NIR photon. Through the integration of upconversion material with semiconductor, low energy visible–NIR light can be absorbed and then emitted as upconverted higher UV–visible energy photon that can excite the neighboring photocatalysts with large bandgap for electron–hole pair generation, and thus completes the photocatalytic cycle. The most commonly used upconversion materials in photocatalysis are lanthanides (Ln) and carbon dots (CDs). The upconverted spectra can range from UV to visible light based on the selectable phosphor hosts and compositions of Ln compounds, as well as the tunable size, surface states, and doping atoms of CDs, which make long-wavelength visible–NIR irradiation more feasible for overcoming the drawback of large bandgap semiconductors. Simultaneously, energetic charge carriers are generated with high redox potential to boost the photocatalytic reactions.

In the Ln upconversion, two basic upconversion mechanisms are involved: excited-state absorption (ESA) and energy transfer upconversion (ETU).[91,92] ESA is a single-ion-based process observed for low doping concentration (<1%), whereas in the case of ETU, it always involves at least two ions, possibly different types of ions, with high concentrations. ETU is by far the most efficient upconversion process in Ln-based upconversion systems. The fascinating spectral conversion of the Ln elements arises from their unique electronic structure of [Xe] $6s^2 4f^n$ (n = 0–14). By virtue of the partly filled 4f shell, the n electrons in 14 available orbitals have 14 over n possible configurations, which give rise to rich energy levels for photon management.[91,92] Moreover, the dipole-forbidden nature of the 4f–4f transition endows the Ln with long decay lifetimes in the order of microseconds, which increase the probability of sequential excitations and excited state energy transfer of the Ln ions.[91,92] The host matrix of Ln-based upconversion system has important influence on the conversion efficiency. Fluorides, including $NaYF_4$, $NaGdF_4$, and CaF_2, are the most popular matrixes for Ln elements due to their high refractive indices and transparencies originating from the low-energy phonons.[93] Moreover, the dopant compositional combinations, such as Yb/Er, Yb/Tm, and Yb/Ho, of the Ln elements are also crucial for the luminescence emission.[93] The wavelength and relative intensity of emitting peaks can be tailored by altering the types and proportions of Ln ions. Consequently, the upconversion of Ln compounds is able to excite semiconductors with different bandgaps (Figure 8d), which has been proven by many researches.

For instance, Zhang and Hong have synthesized a core–shell structured $NaYF_4$:Yb,Tm@TiO_2 photocatalyst via the coating of anatase TiO_2 nanocrystals on the $NaYF_4$:Yb,Tm rods.[94] Under 980 nm laser irradiation, the upconversion $NaYF_4$:Yb,Tm rods emit strong UV and blue light. With the coating of TiO_2 on the $NaYF_4$:Yb,Tm surface, notable spectral differences are observed. The emission peak in the UV region of the $NaYF_4$:Yb,Tm@TiO_2 composite is significantly decreased compared to that of the bare $NaYF_4$:Yb,Tm nanorods, indicating that the UV photon energy generated by the upconversion process of $NaYF_4$:Yb,Tm is absorbed by the TiO_2 (Figure 8e,f). On the contrary, the emission intensities at the blue region of the $NaYF_4$:Yb,Tm@TiO_2 are slightly suppressed likely due to the shielding effect of TiO_2 since the energy is insufficient to excite TiO_2. Ln element–induced upconversion visible–NIR capture has been validated by many reports through the construction of diverse upconversion/semiconductor composites, including a great number of binary $NaYF_4$:Yb,Tm@TiO_2 composites with different structures,[95–97] $NaYF_4$:Yb,Tm–BiOCl nanosheets,[98] $ZnWO_4$:Er,Tm,Yb–BiOI,[99] $NaGdF_4$:Yb,Tm@TiO_2,[100] $NaYF_4$:Yb,Tm@ZnO,[101] $BiVO_4/CaF_2$:Er,Tm,Yb,[102] $NaYF_4$:Yb,Er/Au/CdS,[103] $NaYF_4$:Yb,Er,Tm@TiO_2–Au,[104] and so on.

On the other hand, CDs including carbon nanodots (CNDs) and graphene quantum dots (GQDs), as inexpensive, abundant and benign carbon nanostructure of less than 10 nm in diameter, are newer upconversion materials.[105] The light absorption of the CDs is grounded on the photoexcitation of conjugated π-electrons in the sp^2 carbon network of the core carbon nanoparticle.[106] CDs exhibit broad upconversion absorption ranging from the UV–visible to the NIR region, and large cross section of the emission range. Their fluorescence emissions can be shifted based on the excitation wavelength,[107] size distribution of the CDs, surface functional groups, and emissive traps of intrinsic defects.[108] Additionally, the upconversion efficiency of the CDs can be further optimized through tuning heteroatom doping and surface states, which enables the upconversion properties of CDs adjustable.[105,107] Importantly, by integration with electron acceptor, the upconversion photoluminescence (PL) can be efficiently quenched accompanied with energy transfer, which provides a firm foundation for judicious design of long-wavelength visible–NIR light responsive photocatalysts. Various energy bandgaps of semiconductor-based photocatalyst can be accommodated by CDs to expand the absorption range, covering a significant portion of the solar irradiation.[93]

Kang and co-workers have reported the harnessing of NIR light over CNDs/Cu_2O photocatalytic system through the upconverted PL property of CNDs.[109] The CNDs absorb the long-wavelength NIR light (λ > 700 nm) and emit shorter wavelength light in the range of 390–564 nm as a result of upconversion, which can be subsequently absorbed by Cu_2O to generate active electron–hole pairs. Consequently, the CNDs/Cu_2O composites show high photocatalytic activities under NIR light irradiation. Dong and co-workers have constructed a N-doped carbon dots (NCDs)/Bi-Bi_2MoO_6 photocatalyst for the capture of NIR light to enhance the photocatalytic activity.[110] The NCDs can achieve an upconversion of light from 705–862 nm to a shorter wavelength of 350–500 nm. When the NCDs are integrated with Bi-Bi_2MoO_6, the composite efficiently converts NIR light to visible light and stimulates the Bi-Bi_2MoO_6 to generate charge carriers. Under the 750, 800, and 862 nm light irradiation, the NCD/Bi-Bi_2MoO_6 hybrids display strong characteristic PL emission peak of Bi_2MoO_6 at around 470 nm, which attests the upconversion of NCDs for activating Bi_2MoO_6 in the NIR range.

In spite of the popularity of employing upconversion mechanism to promote the visible–NIR photon harvesting, the solar light conversion efficiency is far from practical application because of some well-known limitations. For the Ln-based upconversion crystals, the narrow light absorption range in the visible–NIR spectrum and the low luminescence efficiency greatly restrict the applicability of this strategy for solar light

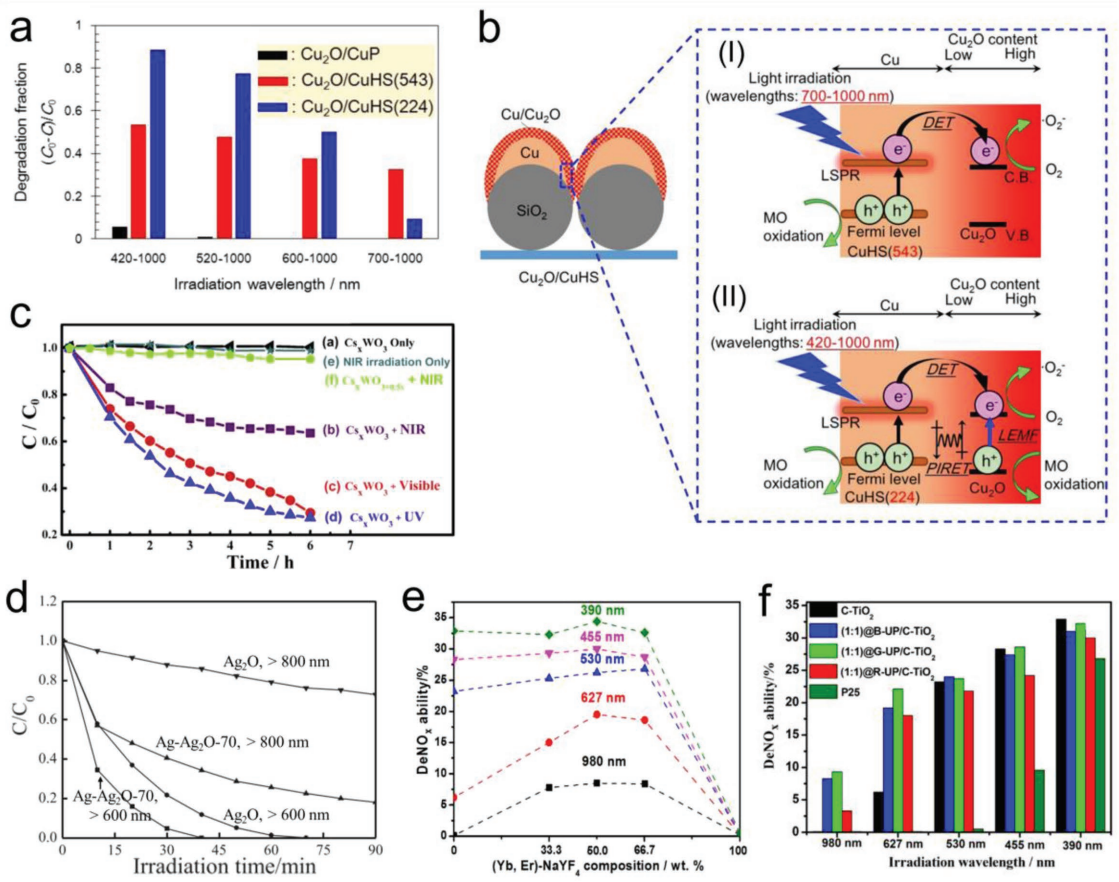

Figure 9. a) Dependence on the irradiation wavelengths of the photocatalytic degradation of MO in the presence of Cu_2O/CuP (Cu plate without SPR absorption), Cu_2O/CuHS(543), and Cu_2O/CuHS(224); b) proposed mechanisms of photodegradation of MO. a,b) Reproduced with permission.[128] Copyright 2017, American Chemical Society. c) Photocatalytic activity in degradation of MB under different conditions over Cs_xWO_3. Reproduced with permission.[129] Copyright 2016, Elsevier. d) Temporal course of photodegradation of 2-CP in aqueous dispersions of Ag_2O and Ag–Ag_2O-70 at >600 and >800 nm light irradiation. Reproduced with permission.[131] Copyright 2015, Elsevier. e) Photocatalytic degradation of NO_x over (Yb,Er)-$NaYF_4$/C-TiO_2 composites with different (Yb,Er)-$NaYF_4$ content under diverse light irradiation. Reproduced with permission.[132] Copyright 2013, Nature Publishing Group. f) NO_x destruction activities of C-TiO_2, B-UP/C-TiO_2, G-UP/C-TiO_2, R-UP/C-TiO_2, and P25 under the irradiation of different wavelengths of light. Reproduced with permission.[133] Copyright 2014, Elsevier.

photocatalysis. In addition, the present reported Ln–semiconductor photocatalyst system normally employs one semiconductor to couple with the upconversion crystal. However, the Ln-based upconversion PL spectra contain multiple sharp emissions, in which the wavelength varies from UV to visible containing purple, blue, and green luminescence peaks. In most cases, the coupling of one semiconductor, particularly for the large bandgap semiconductor such as TiO_2, only harnesses the upconversion emission peak in the UV region, whereas the emissions in the blue and green regions are not absorbed. This results in the insufficient utilization of the converted light and lowers the solar energy conversion efficiency. In view of the limitations, the design of upconversion photocatalyst system with broader light absorption, higher conversion, and utilization efficiency under low light irradiance is needed. This can be potentially achieved through i) constructing multiple Ln element hybrid upconversion crystals to extend the light absorption range; ii) epitaxial coating of the upconversion crystal with semiconductor shell to form hierarchical core–shell structure, which can passivate the surface defects of upconversion crystals and result in obvious enhancement in overall upconversion emission intensity and lifetime, and moreover, the core–shell structure can also improve the photon capture and confinement to enhance light absorption; and iii) employing more semiconductor or other light-active component to fabricate multinary composite. This will fully harness the upconverted light and simultaneously promote the photoexcited electron–hole separation via the charge transfer between the light-responsive components.

As for the CD-based upconversion system, it is not limited by specific light wavelength absorption and display broader light absorption range than Ln elements. However, the flexible function of CDs in photocatalysis is a critical obstacle that complicates the study on the role of CDs and hinders the development of this type of material. Specifically, besides the upconversion function, the CDs can also behave as photocatalyst by itself to generate electron–hole pairs. In combination with semiconductor, it is hard to distinguish the origin of the broad-spectrum photoactivity of the CD-based material system, whether it is from the upconversion mechanism or the direct photoinduced

charge carrier generation mechanism. Moreover, the primarily reported synthesis of CDs follows a bottom-up method by carbonization of organic molecules, polymers, or other carbon-rich precursors. The process is convenient and versatile, but less controllable, yielding CDs with wide size distribution and diverse nanostructure, which results in varied optical properties. This poses additional hurdles for the photocatalytic mechanistic study of CDs. In this respect, synthesizing well-defined CDs with narrow size distribution by a top-down strategy such as electrochemical etching of carbon nanotubes and graphene offers great potential to solve the problem. Moreover, the utilization of monochromatic light with different wavelengths is also a powerful approach to confirm the working mechanism of CDs in the long-wavelength visible–NIR photon capture. The tunable optical response of the CDs over a wide range of wavelengths deserves more research attention.

3.4. Photothermal Materials

Different from the narrow optical gap, photosensitizer, and upconversion materials for photo-to-charge and photo-to-photo transformation, the photothermal material is used for photo-to-thermal conversion. The photothermal effect has been widely studied in biomedical thermal therapy for killing cancerous cells directly using the thermal energy generated. It is produced by photoexcitation resulting in partial or complete thermal energy (heat) generation, which can be observed in various materials such as metals, semiconductors, carbon-based materials, and conjugated polymers. In photocatalysis, the reaction is driven by light as the electron–hole pairs are generated by photon energy rather than thermal energy. Thus, heat alone usually cannot lead to photocatalytic reaction using a semiconductor-based photocatalyst,[111] and the photothermal effect in this case plays an auxiliary role in improving the photocatalytic activities.

Upon light irradiation, photothermal materials absorb broad solar spectrum and generate heat that subsequently dissipate to the surrounding. This effect can induce temperature rise in microscopic and/or macroscopic levels due to confined heat at the immediate surrounding of the photothermal materials and collective bulk heating of the system, respectively. The impact of increasing temperature on photocatalysis can be a collective effect of multistage processes, including changes in charge carrier mobility, Gibbs free energy, mass transport of reactants, and adsorption–desorption rate depending on the temperature regime.[111–113] In general, the increase in reaction temperature leads to lower apparent activation energy of photocatalysis that results in thermal acceleration of the reaction and improved the photocatalytic reactivity rate. Adopting nanomaterials as photothermal materials in photocatalysis has a few advantages: i) efficient harvesting of sunlight especially in the NIR region, ii) elimination of an external thermal energy input, iii) controllability in the location of a chemical reaction down to the nanoscale, and iv) confining heating region that improves the heating dynamics due to low heat loss and reduced thermal mass.

Currently, the extensively used photothermal material is metal nanoparticle (gold, silver), which exhibits visible–NIR light absorption with noticeable photothermal conversion efficiency. For instance, Ho and co-workers have reported a solar thermal collector of SiO_2/Ag@TiO_2 that possesses efficient photothermic property for photocatalytic application.[10] In the composite, the Ag nanoparticles are enclosed within transparent SiO_2 spheres to isolate them from TiO_2. Under visible–NIR light irradiation, the Ag absorbs photons and results in the excitation of electrons. These generated hot electrons can decay through electron–electron scattering process and release the energy in the form of heat, leading to rapid increase in the local temperature of the immediate surrounding of the metal nanoparticles (Figure 8g). Similar plasmonic metal–induced photothermal effect for broad solar spectrum harvesting has been reported by Wang and co-workers.[114] They fabricated a Ag-loaded Bi_2WO_6 photocatalyst and studied its temperature-dependent photocatalytic activity. Results show that Ag loading could significantly raise the solution temperature under simulated solar light irradiation, while high temperature is confirmed to be beneficial for the photocatalytic performance.

Another group of material investigated for photothermal effect is carbon-based materials. They possess high solar absorbance over the broad spectrum and excellent photothermal conversion efficiency. Moreover, compared with metals, they are cheaper and more abundant.[115,116] Graphene has been extensively studied for photocatalysis due to their large surface area, adsorption of pollutants, and high charge carrier mobility.[13,14,117–121] Recently, graphene is also demonstrated to be an excellent photothermal material for photocatalysis application. Wu and co-workers have reported the photothermal contribution of rGO to enhance the photocatalytic performance of rGO–TiO_2 composite.[42] The rGO with remarkable light absorption in the full solar spectrum displays noticeable photothermal conversion property. NIR irradiation results in a favorable temperature increase of the photocatalytic reaction system through heating up the rGO sheets (Figure 8h), which consequently enhances the photoactivity and promotes the solar energy utilization efficiency of the rGO–TiO_2. Neelgund and Oki have also reported the photothermal effect of graphene in promoting solar energy capture through construction of rGO–ZnO nanocomposites.[122] They disclose that the heat generated by NIR light absorption over graphene could remarkably increase the local temperature of the photocatalytic mixture even under the condition of constant circulation of water. The solar heating speeds up the separation and transfer of photogenerated charge carriers, and thus results in the photoactivity enhancement of rGO–ZnO.

Moreover, some nonplasmonic metals such as bismuth[123] and metal oxides such as Fe_3O_4[124] and CuO[19] have also been reported as photothermal materials to promote solar energy utilization for photocatalysis. Ye and co-workers have developed the utilization of semimetal bismuth to capture the NIR light for solar thermal promoting the photocatalytic activity of $Bi_4O_5I_2$.[123] Wu and co-workers have proven the harvesting of NIR light energy by a core–shell-structured Fe_3O_4@SiO_2 to promote the photocatalytic activity of a series of classical TiO_2, g-C_3N_4, BiOI, and CeO_2 photocatalysts.[124] Together, these reports consolidate that photothermal effect plays an important role in promoting solar energy conversion. Moreover, there are also some examples of incorporating photothermal materials with thermocatalytic activity such as Pt,[125] CeO_2,[126]

and $CeMn_xO_y$[127] into a photocatalytic material for synergetic enhancement of the overall photothermal catalysis process. For such cases, the photothermal materials essentially function as thermal catalyst which will not be included here.

In short, coupling solar thermal effect with photocatalysis has been a key concept in solar energy utilization, which offers a promising way to harness the whole solar spectrum by optimization of the photothermal material with high conversion efficiency. At present, the study on solar thermal promoted photocatalysis is increasing, but the energy conversion efficiency is mainly limited by the following two factors that cannot be both optimized in the existing photothermal catalyst system: i) relatively narrow range of light absorption and/or low absorption coefficient of the solar thermal material, and ii) low content of the solar thermal material in the composite system. For instance, metal and metal oxide generally harness part of the solar energy with moderate absorbance, which is far from full absorption in the entire spectrum. Employing carbon materials such as graphene is efficient for resolving the first limitation, but not the second one. This is because all the currently studied solar thermal materials, including metal, metal oxides, and carbon materials in solitary, are generally inactive for photocatalysis. They need to integrate with light-active semiconductor to construct hybrid system. As a result, the weight content of these materials in the hybrid composite is mostly below 10 wt% owing to the possible detrimental effects such as low yield and/or high recombination of charge carriers engendered at high content.

In this context, for enhancing the solar energy capture through the solar thermal-promoted photocatalysis approach, the fabrication of high-efficiency photothermal catalyst system with intense and broad solar light absorption while asserting the generation of photogenerated carriers with high redox ability is essential. Delicate designs of the nanostructures such as the collective effect of nanoparticle assemblies and the optical cavity of hollow nanostructures are promising ways to realize this goal. Additionally, controlled disorder engineering of light-active material to introduce small new gap states provides new opportunity to enhance the solar utilization. In the disorder-rich nanostructure, the retained crystalline structure can inherit the original photocatalytic property of the material for generation of charge carriers, while the disorder region can induce new light absorption in the whole solar spectrum for solar heating. Consequently, full spectrum harvesting of the solar energy for photocatalytic application can be expected.

4. Photocatalytic Purification and Solar Fuel Production

Direct utilization of solar energy to degrade persistent pollutants is an ideal green way for environmental remediation, while the solar-to-fuel conversion is a "Holy Grail" for clean renewable energy production. The bifunctionalities of photocatalysis are of great significance toward the realization of a sustainable society. In this part, we focus on the review of the progress in long-wavelength visible–NIR driven environmental-energy arena, i.e., solar fuel production of H_2 from water, carbon-based fuel (e.g., CO, CH_4) generation from CO_2, and destruction of pollutants for water/air purification. Here, the essential unifying principle of photocatalysis is the use of photoactive catalytic materials to induce chemical reactions upon photon absorption from the visible-to-NIR wavelength.

4.1. Photocatalytic Purification

Photocatalysis is considered as "advanced oxidation process" because of its capability to generate very reactive species such as hydroxyl (•OH) and superoxide radicals ($\bullet O_2^-$) with strong oxidizability. The photocatalytic elimination of pollutants is extensively investigated, by which contaminants are mineralized to less toxic inorganic compounds, such as water, carbon dioxide, and salts. The developments in the engineering of visible–NIR photocatalysts greatly advance the utilization of solar energy. Till now, the reported photocatalytic degradation reactions performed under wide-spectrum visible–NIR light irradiation consist of two types: liquid phase and gas phase degradation. In this section, the progress in this area is presented.

Sugawa et al. have described an efficient visible and NIR light-driven degradation (400–1000 nm) of MO over Cu_2O/Cu plasmonic photocatalysts.[128] They prepared two Cu_2O/Cu half-shell (CuHS) photocatalysts, i.e., Cu_2O/CuHS(543) with SPR absorption peak in the NIR region that is far from the light absorption wavelength of Cu_2O (around <650 nm) and Cu_2O/CuHS(224) with SPR absorption band that partially overlaps with the absorption edge of Cu_2O. Wavelength-dependent photocatalytic performance tests confirm the broad light driven photoactivity of the two Cu_2O/Cu samples (**Figure 9**a). Owing to that the SPR dip of Cu_2O/CuHS(543) centers at a wavelength of 866 nm that is at a much lower energy than the band gap region of Cu_2O, the observed high catalytic activity at around 700–1000 nm is ascribed to the SPR-induced direct electron transfer mechanism (I of Figure 9b). On the other hand, the SPR of Cu_2O/CuHS(224) is centered at a wavelength of 626 nm and its superior photocatalytic activity at 420–1000 nm is proposed to be induced by the combined contribution of the Cu SPR effect and bandgap excitation of Cu_2O (II of Figure 9b). Moreover, Liu and co-workers have realized full-spectrum-response photocatalytic degradation of MB on Cs_xWO_3 nanorod with mixed valence states.[129] As shown in Figure 9c, the removal rates of MB on Cs_xWO_3 nanorod are determined to be 72%, 70%, and 37% under UV, visible, and NIR irradiation within 6 h, respectively. The photoactivity is suggested to origin from the low-valence chromophore of photosensitive W^{5+} sites in the material, which can absorb NIR photon to generate photoelectrons and produce W^{6+}. Subsequently, the photogenerated electrons could be trapped by the absorbed O_2 to form $\bullet O_2^-$ followed by the generation of •OH and •OOH, for degradation of MB. On the other hand, the W^{6+} sites can react with OH^- and restore to W^{5+}, realizing a close-loop photocatalytic reaction.

Besides the organic dyes, other commonly hazardous wastes that have been studied for photocatalytic water purification are the phenolic compounds and antibiotics. Dong and co-workers have evaluated the photocatalytic degradation of tetracycline (TC) in water under visible and NIR light ($\lambda > 700$ nm) irradiation using nitrogen-doped GQD (NGQD)-modified Z-scheme g-C_3N_4/Bi_2WO_6 heterojunctions.[130] The degradation rate of

TC over the NGQD-C_3N_4/Bi_2WO_6 reaches up to about 29.8% after 180 min, which is far higher than the 4.4% of the C_3N_4/Bi_2WO_6 heterojunction. The high photocatalytic performance of NGQD-C_3N_4/Bi_2WO_6 arises from the upconversion effect of NGQD.[130] Hu and co-workers have demonstrated the degradation of 2-chlorophenol (2-CP) under visible and NIR light irradiation in the presence of wide-spectrum response Ag–Ag_2O photocatalyst.[131] As shown in Figure 9d, 2-CP is completely degraded over the Ag–Ag_2O-70 sample within 40 min under the light irradiation of $\lambda > 600$ nm. In addition, under the light illumination of $\lambda > 800$ nm, 82% of 2-CP can be removed by Ag–Ag_2O-70 within 90 min. Since the SPR of Ag NPs is located at ≈400–600 nm, it is apparent that the photocatalytic activity of Ag–Ag_2O originates from the photoexcitation of Ag_2O based on its small bandgap. The metallic Ag enhances the electron–hole separation due to its electron trapping effect.

In comparison with the abundant studies on harvesting broad visible–NIR photon for the photocatalytic elimination of pollutants in liquid phase, there are only several reports on the visible–NIR light driven photocatalytic removal of gaseous pollutants. Most of which are focused on the removal of NO_x, a main pollutant that contributes to the acid rain formation. Yin and co-workers have reported the destruction of NO_x gas under the irradiation of UV to NIR light over a Yb,Er-$NaYF_4$/C-doped TiO_2 (C-TiO_2) photocatalyst.[132] In the composite, NIR light excites Yb,Er-$NaYF_4$ upconversion phosphor and UV–visible light drives C-TiO_2 photocatalyst. Consequently, the Yb,Er-$NaYF_4$/C-TiO_2 displays wider spectrum photoactivities than the solely C-TiO_2 (Figure 9e). In a subsequent work of the group, they have tested the UV to NIR photocatalytic destruction of NO_x gas over other blue Yb,Tm-$NaYF_4$ (B-UP) and red color Yb,Er-Y_2O_3/YOF (R-UP) emitting upconversion phosphor coupled C-TiO_2 composites, and compared their photoactivities with green Yb,Er-$NaYF_4$ (G-UP) coupled C-TiO_2.[133] The G-UP/C-TiO_2 composite presents superior photocatalytic performance than the blue and red ones (Figure 9f), which is ascribed the much stronger emission intensity of green G-UP under the excitation of 980 nm NIR laser.

4.2. Photocatalytic Solar Fuel Production

Solar fuel production is based on the concept of harnessing abundant sunlight energy to drive the chemical reactions that make fuels and store solar energy in the form of chemical bonds. Solar-powered water splitting to generate H_2, a clean and renewable fuel, is the most commonly investigated solar fuel conversion in the literature. Another widely studied solar fuel production reaction involves the photocatalytic reduction of CO_2 to generate carbon-based fuels such as CO, CH_4, and CH_3OH, which offers new sources of energy with neutral CO_2 emission. Traditionally, the potentials needed to initiate the reactions of interest are greater than 1 V because of the presence of thermodynamic barrier for decomposing the stable and chemically inert covalent O—H bond in H_2O and O=C bond in CO_2 molecules and activation barriers for driving the surface chemical reactions. The high energy input requirement imposes great restriction on the visible–NIR photons harvesting due to their low energy at high wavelength. In recent years, benefiting from the advances in material design and the focus on the half-reaction of the H_2 evolution and CO_2 reduction, there is a surge in the reports of photocatalytic solar fuel production at a long visible–NIR wavelength. In this section, some typical examples are selected to highlight the progress in this area.

Majima and co-workers have reported a visible and NIR light-driven photocatalytic H_2 evolution from methanol/water solution catalyzed by Pt-tipped Au NR plasmon material (**Figure 10**a).[40] The sample displays broad photon absorption in the range of 700–1200 nm. The monochromatic light irradiation reveals wavelength-dependent photocatalytic H_2 evolution activity (Figure 10b). The composite reaches 0.51% of apparent quantum efficiency (AQE) at 540 nm and 0.68% at 940 nm light irradiation. Notably, steady AQE can still be obtained even up to 1100 nm. Energy relaxation analysis of the plasmon generated hot electrons directly proves the electron transfer from the excited Au to the Pt at the end of the nanorods, confirming that the H_2 evolution is induced by the photocatalytic SPR process (Figure 10c). In addition, Tang and co-workers have realized the photocatalytic water splitting under NIR-photon irradiation by synthesizing WO_2–Na_xWO_3 ($x > 0.25$) hybrid materials with tunable compositions and optical properties (Figure 10d).[134] The optimal WO_2–Na_xWO_3 with the composition of 37.5% WO_2 and 62.5% Na_xWO_3 displays an absorption energy gap of ≈1.10 eV, corresponding to a light absorption spectrum of ≈1129 nm. The hybrid composite exhibits H_2 evolution from phosphate-buffered saline without sacrificial agent under 980 nm laser light illumination (Figure 10e). The IR-driven photocatalytic water splitting ability is proposed to originate from the energy bands overlapping between the metallic WO_2 and Na_xWO_3, which forms an exquisite ladder-type carrier transfer process (Figure 10f).

Besides the advances made in the wide-spectrum photocatalytic H_2 evolution through half-reaction, a recent breakthrough in long-wavelength photon capture for overall water splitting has been reported by Yang and co-workers.[135] They introduced a black metallic tungsten nitride (WN) with an absorption energy gap of 1.55 eV for overall water spitting at wide light wavelengths from 300 to 765 nm (**Figure 11**a). As illustrated in Figure 11b, the band structure of WN is comprised of partially occupied CB (–4.7 eV to Fermi level), continuous unoccupied band B_1 above the Fermi level, and two bands below the CB (B_{-2} from −20 to −16 eV with mainly N 2s states, and B_{-1} between −11 and −4.7 eV with strongly hybridized W 5d and N 2p states). The energy through interband transition from CB to B_1 is greater than the minimum theoretical energy required for the water splitting (1.23 eV), which enables the photogeneration of redox electron–hole pairs to perform water splitting (Figure 11c).

In photocatalytic CO_2 reduction, Ye et al. have reported an efficient photoreduction of gas phase CO_2 into solar fuels under visible–NIR light over an olive-green few-layered BiOI with expanded spacing of the (001) facets and V_o.[136] Under the light irradiation of $\lambda > 420$ nm, CO and CH_4 are generated at the rates of 0.615 and 0.063 μmol h^{-1}, respectively. With the light irradiation of $\lambda > 700$ nm, the corresponding generated CO and CH_4 are about 0.119 and 0.021 μmol h^{-1} (Figure 11d). Moreover, the AQEs for the solar fuel (CO and CH_4) production over the few-layered

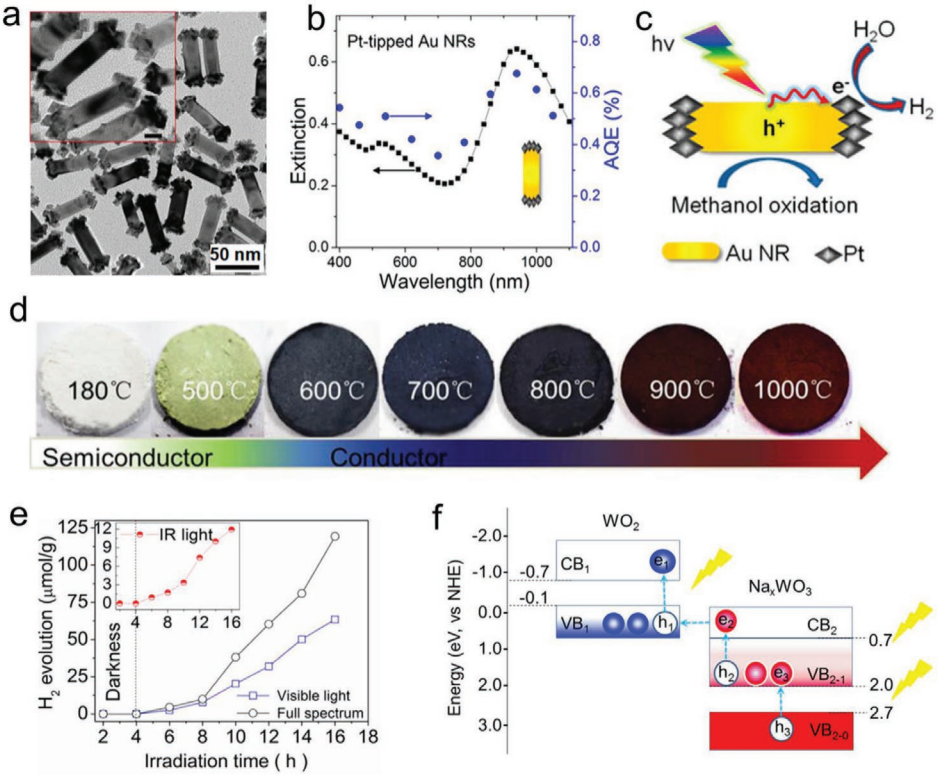

Figure 10. a) TEM images of Pt-tipped Au NRs; b) extinction spectra and AQE of Pt-tipped Au NRs; c) schematic diagram for H_2 production reaction mechanism of Pt-tipped Au NRs. a–c) Reproduced with permission.[40] Copyright 2014, American Chemical Society. d) Color change for the different WO_2–Na_xWO_3 samples at increased calcination temperatures; e) photocatalytic H_2 evolution rates for optimal WO_2–Na_xWO_3; f) energy-level diagrams of WO_2–Na_xWO_3. d–f) Reproduced with permission.[134] Copyright 2015, American Chemical Society.

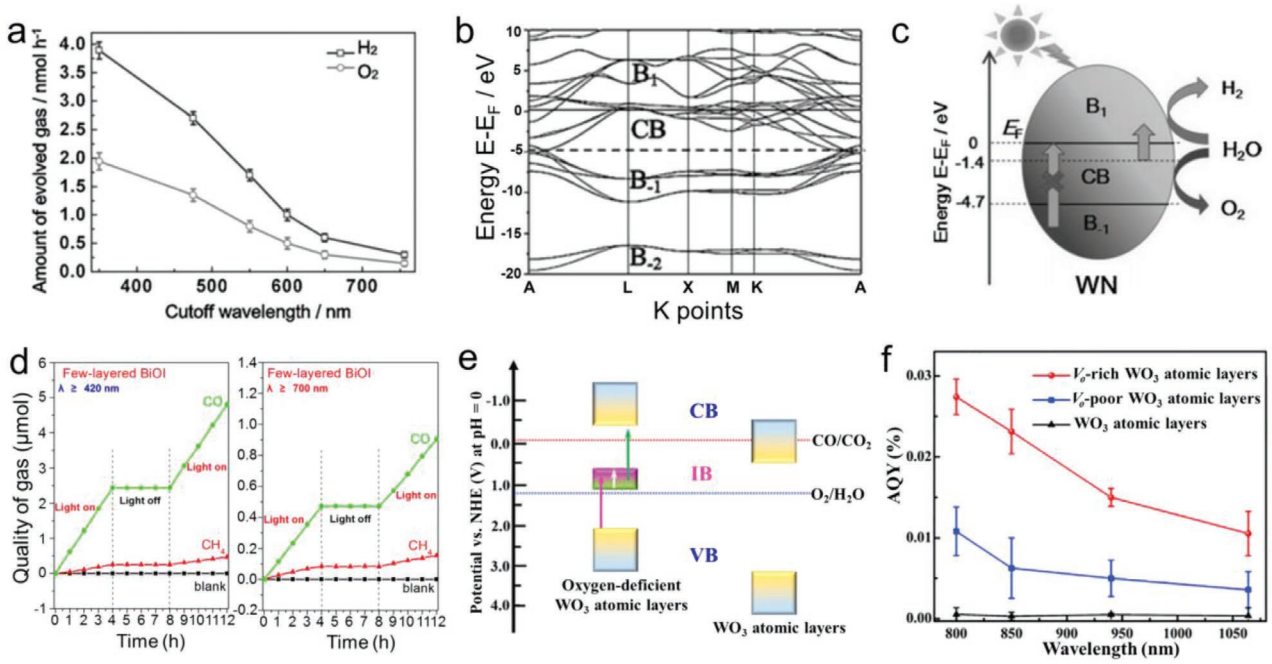

Figure 11. a) The dependence of the H_2 and O_2 evolution rates from pure water on the cutoff wavelength of incident light; b) calculated band structure of WN; c) possible photoexcitation process in WN. a–c) Reproduced with permission.[135] Copyright 2017, Wiley-VCH. d) Photocatalytic produced CO and CH_4 gases under different light irradiation over few-layered BiOI. Reproduced with permission.[136] Copyright 2016, Elsevier. e) Scheme of the electronic band structure of oxygen vacancy (V_o)-rich WO_3; f) AQE test of CO_2 photoreduction under different light wavelengths for the V_o-rich WO_3, V_o-poor WO_3, and WO_3. e,f) Reproduced with permission.[24] Copyright 2018, Elsevier.

BiOI under 420 and 700 nm monochromatic light irradiation are 0.14% and 0.02%, respectively. Very recently, Xie and co-workers have reported exceptionally wide NIR-driven CO_2 overall splitting into hydrocarbons and O_2 in the presence of H_2O on a single ultrathin intermediate-band WO_3 semiconductor.[24] In this work, the abundant V_o in WO_3 atomic layers largely extends the light response to IR light up to 10 000 nm. Theoretical calculations and experimental characterizations disclose that the created V_o reaches a critical density that results in an upshift of the VB and more importantly generates a new intermediate band at ≈0.63 eV below Fermi level in the WO_3 atomic layers. The oxygen-deficient WO_3 atomic layers are able to potentially realize carrier transitions from the VB to the empty intermediate-band states. Other possibilities include carrier transitions from the occupied intermediate-band states to the CB state, as well as transitions within the partially filled intermediate band can also occur (Figure 11e), hence achieving IR-driven CO_2 overall splitting. The AQE test in the range of 800–1064 nm demonstrates that the oxygen-deficient WO_3 atomic layers show quantum efficiencies up to 1064 nm, while the pristine WO_3 atomic layers exhibit negligible quantum efficiencies above 800 nm (Figure 11f). Moreover, $^{13}CO_2$ labeling experiment ascertains that the evolved CO indeed derived from the photoreduction of CO_2.

5. Solar Thermal Promoted Photocatalytic Purification and Fuel Production

As discussed earlier, diverse methods have been developed to extend the absorption range of the photocatalysts from UV to visible and NIR light, such as electronic structure modification of the semiconductors, loading photocatalysts with sensitizer, and conversion of low-energy light to high-energy light through upconversion process. However, the photons absorbed and utilized for the photocatalytic reaction by these composite photocatalysts are still insufficient. Majority of the photons that are not absorbed by the photocatalyst are converted to heat resulting in a rise of the reaction medium (water or gas) and/or photocatalyst temperature. Even if the photons are absorbed by the photocatalysts, a fraction of them actually release their energy as heat through some processes, such as molecular vibration in organic materials, plasmonic heating in noble metals, and recombination process in semiconductors. Nevertheless, this photothermal effect has often been overlooked in most photocatalytic reactions previously.

In recent years, incipient investigation of photothermal effect on photocatalysis has evolved. The development of photothermal nanomaterials as heat nanogenerator greatly enhances the solar thermal contribution in catalytic reactions. The increase in temperature caused by the photothermal nanomaterials at the immediate surrounding of the photocatalyst confines the heat at the specific reaction site to achieve localized heating effect. This effect has been reported to enhance the photocatalytic reaction through multiple ways, such as promoting the diffusion of reactants,[137] improving the mobility of photogenerated charge carriers,[42,122] promoting the transfer of intermediates at the surface of the catalyst,[113] prolonging the lifetime of photogenerated carriers,[19] and lowering the activation energy for the redox reaction.[138,139]

Currently, the solar thermal promoted catalysis is mainly based on two system configurations namely discrete and collective (**Figure 12**a) systems for liquid and gas phase photocatalytic

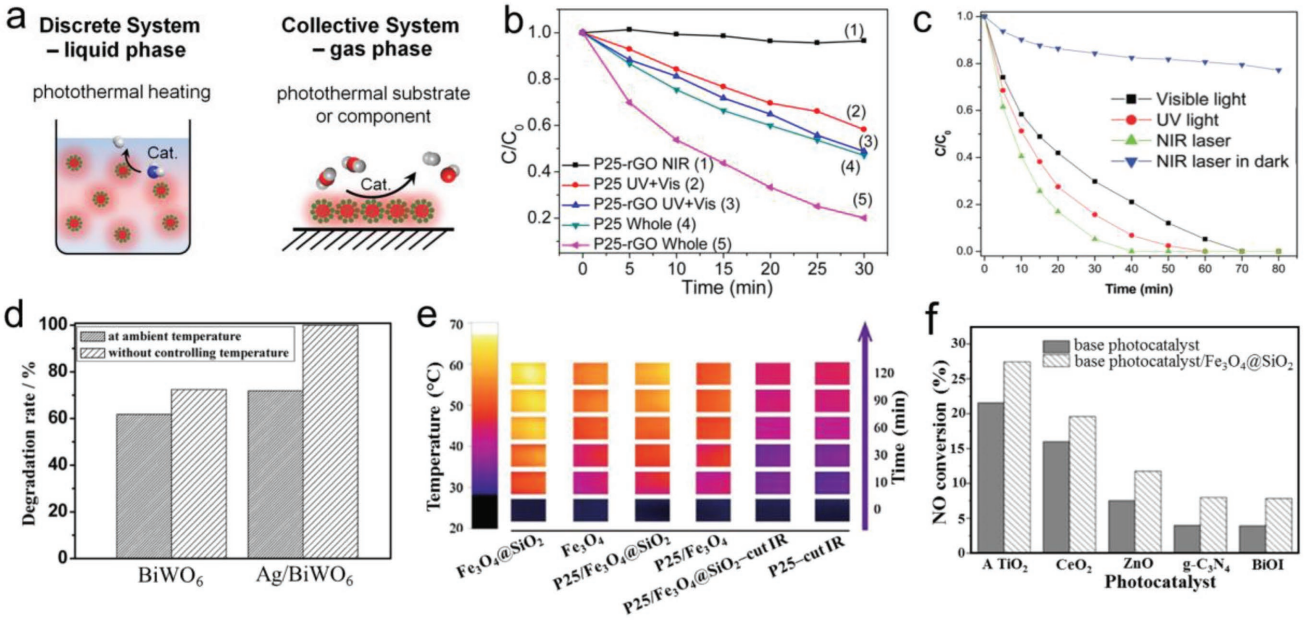

Figure 12. a) Classification of solar thermal promoted photocatalysis. b) Photocatalytic degradation of MB on P25 or P25–rGO. b) Reproduced with permission.[42] Copyright 2014, American Chemical Society. c) Photodegradation profile of MO in the presence of the rGO–ZnO under UV light, visible light, and NIR laser irradiation. Reproduced with permission.[122] Copyright 2018, Royal Society of Chemistry. d) Comparison of degradation efficiency of phenol by Bi_2WO_6 and Ag-loaded Bi_2WO_6 with and without controlling the reaction temperature under light irradiation. Reproduced with permission.[114] Copyright 2012, American Chemical Society. e) Thermal images of various samples upon light irradiation; f) promotion of photocatalytic activity for different photocatalysts. e,f) Reproduced with permission.[124] Copyright 2017, Elsevier.

reactions, respectively. In discrete system, photocatalysts are often dispersed uniformly in solutions, and the photothermal materials serve as heat generator at the reaction interface which leads to an increase in the localized temperature around the composite. Successively, the generated heat will dissipate to the surrounding and heat up the solution to a certain extent. Moreover, since liquid phase is concerned, the temperature of the solution should not exceed the boiling point of water or sacrificial reagent whichever is lower. In the case of collective system in which the photocatalytic reaction occurs in gas phase, the photothermal materials convert the light energy absorbed into heat and cause an increase in temperature on the surface of the photocatalysts. In the gas phase system, such temperature can reach a few hundred Celsius degrees especially when the reaction is performed under air-tight condition with good thermal insulation. In this section, we review the current progress of solar thermal promoted photocatalytic applications in pollutant purification and fuel production.

5.1. Solar Thermal Promoted Photocatalytic Purification

Solar thermal promoted photocatalytic decomposition of pollutants in both liquid phase and gas phase have been proven, which are of great significance in practical solar-driven waste treatment. An increase in temperature of the photocatalytic reaction system affects both the kinetic and the activation energies of the purification process. Wu and co-workers have for the first time investigated an efficient harnessing of NIR light over graphene to thermally promote photocatalytic degradation MB over TiO_2–rGO composite using different light wavelengths (Figure 12b).[42] The results reveal that photoexcitation of electrons in TiO_2 photocatalyst cannot take place with NIR radiation without the presence of UV–visible light. However, with the disposition of NIR light, the photocatalytic activity of TiO_2–rGO under UV–visible light is significantly improved. In this case, NIR light is absorbed by the graphene for photothermal heating, which causes the photogenerated electrons from bandgap excitation of TiO_2 to be more energetic along with enhanced mobility on the hot rGO sheets, thus enhancing the photoactivity of TiO_2–rGO. Moreover, Neelgund and Oki have reported the photothermal contribution of graphene on enhancing the photoactivity of ZnO for degradation of MO (Figure 12c).[122] The addition of NIR radiation in the presence of both UV and visible light leads to an increase in temperature that facilitates the transfer and separation of photogenerated charge carriers. The photothermal conversion efficiency of rGO–ZnO is calculated to be 48.6%. Here, graphene nanosheet functions as both the photothermal material for heat generation and change transfer medium in view of its lower Fermi level relative to ZnO.

Besides, metallic material with high photothermal conversion efficiency for accelerating the photocatalytic degradation reaction has also been reported. Zhang et al. have investigated the solar heating effect of Ag nanoparticles in Ag-loaded Bi_2WO_6 for enhancing the photocatalytic decomposition of phenol.[114] Significant increase of reaction temperature in the presence of Ag-loaded Bi_2WO_6 (from 12 to 68 °C) is observed after 120 min light irradiation, which is much higher than that of Bi_2WO_6 (from 12 to 48 °C). Photoactivity tests show that without controlling the reaction temperature, the improvement in photocatalytic degradation activity of the Ag-loaded Bi_2WO_6 compared to Bi_2WO_6 is also much higher than that under the controlled reaction temperature (Figure 12d). This is ascribed to the synergistic electronic modulation and photothermal effect of Ag nanoparticles, demonstrating that besides the charge trapping, solar thermal conversion of Ag is another important factor that contributes to enhancing the photoactivity.

In the gas-phase reaction, photocatalysts are commonly coated on a substrate. The collective heating effect by the closely packed nanomaterials will cause a rapid increase in the surface temperature of the substrate. Merely by physical mixing of the photothermal materials with the photocatalysts, the solar thermal effect is established due to the collective heating and fast heat dissipation through the surface of the entire substrate. Hu et al. have synthesized Fe_3O_4@SiO_2 core–shell structure as the photothermal material to capture NIR light and mixed with P25 to promote the photocatalytic oxidation activity of NO. The surface temperature of the sample rises from 25 to 59.7 °C in 120 min under UV–vis–NIR light irradiation (Figure 12e).[124] The rate of photocatalytic oxidation of NO increased by 38.9% compared to pure P25. A few experiments have been designed to investigate the enhancement in photocatalytic activity in the presence of Fe_3O_4@SiO_2. First, it is found that the difference in photocurrent intensity between P25/Fe_3O_4@SiO_2 and pure P25 is minimal under UV–vis–NIR light irradiation. This indicates that the presence of Fe_3O_4@SiO_2 does not promote the photogenerated charge carriers. Second, there is a positive relationship between the temperature rise and the amount of Fe_3O_4@SiO_2 used. Lastly, controlled experiments performed under different reaction temperature with P25 indicate that the optimal temperature is 60 °C which matches to the temperature obtained by the optimal P25/Fe_3O_4@SiO_2 sample (59.7 °C). Together, the results consistently confirm that the enhancement in photocatalytic activity is attributed to the photothermal effect of the Fe_3O_4@SiO_2. In addition, other photocatalytic materials have also been mixed with Fe_3O_4@SiO_2 for oxidation of NO, which reveal universal improvement of photocatalytic activities (Figure 12f).

5.2. Solar Thermal Promoted Photocatalytic Fuel Production

Besides pollutant purification, solar thermal enhanced fuel production through water splitting and CO_2 reduction has also been reported. Ho and co-workers have examined the photothermal effect of CuO, which is also a cocatalyst, loaded on TiO_2 nanotubes for enhancing H_2 generation toward efficient utilization of the whole solar spectrum.[19] The highest AQE for light to H_2 conversion achieved by the optimized CuO-loaded TiO_2 nanotubes is about 6 times higher at 90 °C (66.9%) than at 25 °C (10.3%) obtained under UV light. The authors attribute this temperature effect of improved photocatalytic H_2 generation to a longer electron lifetime associated with an enhanced hole scavenging effect of glycerol. Importantly, the as-prepared sample displays a H_2 production rate of 105 mmol g^{-1} h^{-1} at a near boiling temperature of the solution (≈93 °C) under the real Sun with a simple parabolic concentrator (**Figure 13**a).

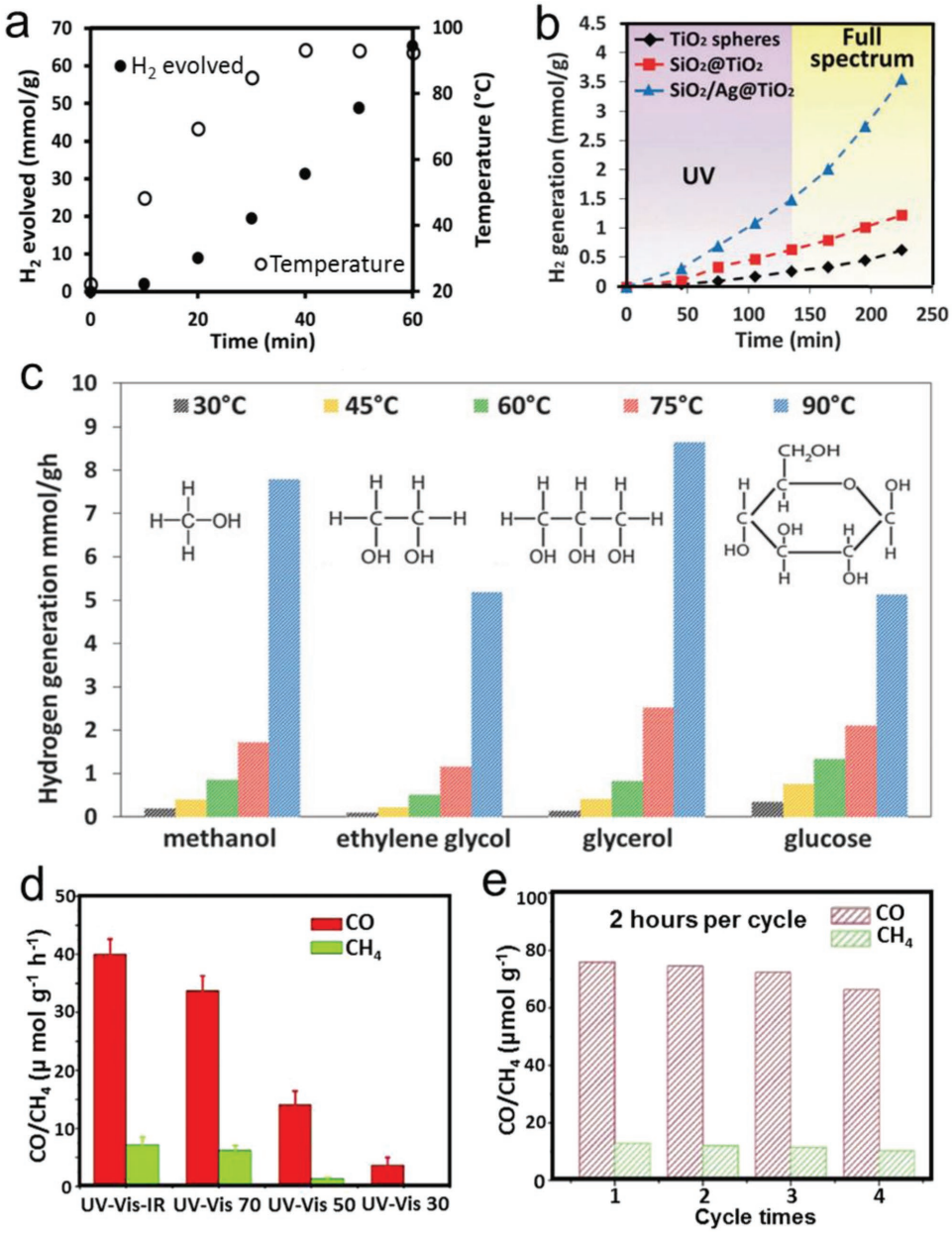

Figure 13. a) H_2 generation by CuO-loaded TiO_2 under practical solar irradiation with a light concentrator. Reproduced with permission.[19] Copyright 2015, Royal Society of Chemistry. b) H_2 generation of TiO_2 spheres, SiO_2@TiO_2, and SiO_2/Ag@TiO_2 core–shell nanocomposites in glycerol–water solution under both UV light and full spectrum irradiation; c) H_2 generation by TiO_2 spheres in different sacrificial reagents at different temperatures. b,c) Reproduced with permission.[10] Copyright 2016, Royal Society of Chemistry. d) Rates of CO and CH_4 under different temperatures over $Bi_4O_5I_2$. e) Cyclic experiment over $Bi_4O_5I_2$ under UV–vis–IR light irradiation for 2 h per circulation. d,e) Reproduced with permission.[123] Copyright 2018, Elsevier.

In a following work, Ho and co-workers further developed a SiO_2/Ag@TiO_2 core–shell nanocomposite for photocatalytic H_2 generation with the SiO_2/Ag function as efficient solar thermal collector based on the visible–NIR-driven heating effect of Ag while the TiO_2 shell absorbs UV light to generate charge carriers.[10] The temperature effect on enhancing the H_2 generation rate is first revealed by elevating the temperature of the TiO_2 photocatalyst from 30 to 90 °C with a series of sacrificial agents of glycerol, ethylene glycol, methanol, and glucose. General increase in the H_2 generation rate is observed for all four sacrificial reagents (Figure 13c). Subsequently, under full solar spectrum, the solar heating effect of Ag renders a notable 95% increment (1536 mmol g^{-1} h^{-1}) in the H_2 generation rate of SiO_2/Ag@TiO_2 as compared with the individual UV light driven H_2 generation activity (Figure 13b). Moreover, Nikitenko et al. have also observed this cooperative effect of light and heat by adopting Ti@TiO_2 core–shell structure as the photocatalyst for water splitting using methanol as the sacrificial reagent.[113] The nonplasmonic metallic Ti core extends the light absorption of the photocatalyst from UV to the NIR region enabling the

bulk temperature of the reaction solution to reach 60 °C. The thermal effect on migration of the intermediates together with the light effect on Ti core for interband transition excitation of electrons leads to consequential photothermal catalytic activity in H_2 production.

In addition, the photothermal effect has also been used in photocatalytic fuel production in terms of CO_2 conversion to chemical energy. Ye and co-workers have developed $Bi_4O_5I_2$ nanosheets incorporated with semimetal Bi spheres for UV–vis–NIR driven solar thermal promoted photocatalysis in gas phase (Figure 13d).[123] The surface temperature of the Bi/$Bi_4O_5I_2$ photocatalyst reaches 79 °C under full spectrum solar irradiation. Specifically, $Bi_4O_5I_2$ nanosheets absorb UV and visible light for photoexcitation of electron–hole pairs, while the NIR light harvested by the Bi promotes the chemical energy production rate due to an increase surface temperature of the photocatalyst. The cyclic test of the as-prepared photocatalyst shows moderate stability (Figure 13e). Here, metallic Bi functions as both a cocatalyst for better charge separation and a photothermal collector for accelerating light to thermal energy conversion. These effects mutually enhance the CO_2 reduction process.

6. Conclusion and Future Perspectives

In summary, we herein present an up-to-date review of the advances achieved in harvesting long-wavelength visible–NIR light for promoting solar energy utilization. The ability to efficiently capture visible–NIR broad spectrum or even UV–visible–NIR full spectrum is clearly a viable route to increasing solar conversion efficiency and in some cases facilitating charge separation-transfer dynamics. This notion witnesses the rapidly increasing and expanding scope of visible–NIR light driven photocatalysis reports. Distinct strategies of utilizing visible–NIR light either to directly trigger photoactivity or convert visible–NIR light to UV–visible light to ignite photocatalysis or otherwise to thermally accelerate photoactivity are discussed. Accordingly, diverse material systems have been progressively engineered to function under long-wavelength visible–NIR light irradiation, which include narrow optical gap, photosensitizers, upconversion, and photothermal materials. The composition and architecture of these classified materials are specifically designed to tune their optical properties and often along with the electronic structure modulation to achieve visible–NIR light absorption and enhanced photogenerated charge separation. These visible–NIR driven catalyst systems have been shown to achieve broad solar energy utilization for conventional photocatalytic and emerging solar thermal assisted photocatalytic pollutant purification in liquid and gas phase, as well as solar fuel production from water splitting and CO_2 reduction. In spite of the achievements reported by different research groups in promoting solar energy utilization, some fundamental issues and challenges remain in this field, which merit further research attention.

In the direct photocatalytic broad solar spectrum utilization, one of the main inherent limitations for efficient full solar spectrum harvesting is the balancing of the photon absorption and charge carrier generation with high redox potential for the photocatalytic activation. This issue is especially rigorous for the narrow optical gap materials. As for the photosensitizers and upconversion crystals, often the discrete light absorption nature of these materials and the required high power of incident light (e.g., laser) greatly limit their practicality and efficiency. The realization of full solar spectrum utilization with high photocatalytic solar energy conversion efficiency is still scanty. Although a large number of reports utilize the keywords of full solar spectrum harvesting/driven or some other similar expression, the absorption from 250 to 2500 nm is generally hard to truly attain. In this context, precise design and hybridization of multiple visible–NIR harvesters within an integral photocatalyst system would be a promising way. For example, the fabrication of metal plasmon and upconversion comodified photocatalyst has shown to display broader light-responsive and higher photocatalytic activity than single upconversion-modified photocatalyst.[104]

On the other hand, in the solar thermal promoted photocatalytic sunlight utilization, the introduction of photothermal material into photocatalyst provides an alternative way to capture broad band solar energy, especially in the infrared region that is a major component of sunlight. Some of the photothermal materials, e.g., carbon-based materials, are able to fully absorb the solar spectrum with high absorbance. Their integration with traditional photocatalyst enables more effective utilization of the solar energy than single-function photocatalyst, while allowing the generation of high redox potential charge carriers. Nonetheless, in the photothermal catalyst system, the solar thermal material is mostly used for accelerating the chemical reactions rather than directly promoting the photoexcitation process for electron–hole pair generation. This stipulates the photothermal materials content in the composite generally on the low side (mostly below 10 wt%). As a result, the solar thermal conversion efficiency is restricted.

Moreover, despite the mainstream reports of solar thermal heating on promoting the photocatalytic activity, negative effect may also arises owing to the multiple steps involved in the solar thermal promoted photocatalytic process. Kim and co-workers have disclosed that the increase in temperature promotes the photocatalytic reaction on the Ag-doped TiO_2 nanoparticles sample, while it shows a negative effect on the nanofibers sample at higher temperature.[140] The reason is ascribed to that the enhanced kinetic energy of the reactants at higher temperature may cause the reactants run away from the active sites of nanofiber before completing the photocatalytic reaction. Furthermore, the complex optical–thermal transformation mechanisms need to be further explored in order to better manipulate the photothermal effect in photocatalysis. Studies on the optimization of materials in terms of photothermal conversion efficiency, reduction of excessive heat loss to the bulk fluid, and reliability and stability under elevated temperature are still limited. Hence, more research effort should be emphasized on in-depth photothermal characterizations and understanding.

Acknowledgements

This work was supported by Ministry of Education (MOE), Singapore, under R-263-000-C85-112 and R-263-000-D08-114 grants.

Conflict of Interest

The authors declare no conflict of interest.

Keywords

environmental purification, fuel production, long wavelength, photo- and photothermal-catalysis, visible–NIR photons

Received: May 6, 2018
Revised: June 8, 2018
Published online:

[1] M.-Q. Yang, N. Zhang, M. Pagliaro, Y.-J. Xu, *Chem. Soc. Rev.* **2014**, *43*, 8240.
[2] C. F. Tan, W. L. Ong, G. W. Ho, *ACS Nano* **2015**, *9*, 7661.
[3] C. Liu, N. P. Dasgupta, P. Yang, *Chem. Mater.* **2014**, *26*, 415.
[4] Z. Luo, T. Wang, J. Zhang, C. Li, H. Li, J. Gong, *Angew. Chem., Int. Ed.* **2017**, *56*, 12878.
[5] D. Kim, K. K. Sakimoto, D. Hong, P. Yang, *Angew. Chem., Int. Ed.* **2015**, *54*, 3259.
[6] N. Armaroli, V. Balzani, *Angew. Chem., Int. Ed.* **2007**, *46*, 52.
[7] X. Liu, J. Iocozzia, Y. Wang, X. Cui, Y. Chen, S. Zhao, Z. Li, Z. Lin, *Energy Environ. Sci.* **2017**, *10*, 402.
[8] M.-Q. Yang, Y.-J. Xu, W. Lu, K. Zeng, H. Zhu, Q.-H. Xu, G. W. Ho, *Nat. Commun.* **2017**, *8*, 14224.
[9] L. Zhu, C. F. Tan, M. Gao, G. W. Ho, *Adv. Mater.* **2015**, *27*, 7713.
[10] M. Gao, P. K. N. Connor, G. W. Ho, *Energy Environ. Sci.* **2016**, *9*, 3151.
[11] J. Wang, G. W. Ho, *Angew. Chem., Int. Ed.* **2015**, *54*, 15804.
[12] L. Zhu, M. Hong, G. W. Ho, *Nano Energy* **2015**, *11*, 28.
[13] M.-Q. Yang, J. Dan, S. J. Pennycook, X. Lu, H. Zhu, Q.-H. Xu, H. J. Fan, G. W. Ho, *Mater. Horiz.* **2017**, *4*, 885.
[14] M.-Q. Yang, N. Zhang, Y. Wang, Y.-J. Xu, *J. Catal.* **2017**, *346*, 21.
[15] M.-Q. Yang, Y.-J. Xu, *Nanoscale Horiz.* **2016**, *1*, 185.
[16] M. Wang, D. Zheng, M. Ye, C. Zhang, B. Xu, C. Lin, L. Sun, Z. Lin, *Small* **2015**, *11*, 1436.
[17] Y. Guo, J. Li, Y. Yuan, L. Li, M. Zhang, C. Zhou, Z. Lin, *Angew. Chem., Int. Ed.* **2016**, *55*, 14693.
[18] C. F. Tan, A. K. Su Su Zin, Z. Chen, C. H. Liow, H. T. Phan, H. R. Tan, Q.-H. Xu, G. W. Ho, *ACS Nano* **2018**, *12*, 4512.
[19] C. K. N. Peh, M. Gao, G. W. Ho, *J. Mater. Chem. A* **2015**, *3*, 19360.
[20] L. Yan, Z. Gu, X. Zheng, C. Zhang, X. Li, L. Zhao, Y. Zhao, *ACS Catal.* **2017**, *7*, 7043.
[21] J. Tian, Y. Sang, G. Yu, H. Jiang, X. Mu, H. Liu, *Adv. Mater.* **2013**, *25*, 5075.
[22] G. Wang, B. Huang, X. Ma, Z. Wang, X. Qin, X. Zhang, Y. Dai, M. H. Whangbo, *Angew. Chem., Int. Ed.* **2013**, *52*, 4810.
[23] J. Zhang, W. Hu, J. Zhang, S. Liu, J. Tong, X. Hou, W. Liu, J. Yang, B. Liu, *J. Phys. Chem. C* **2017**, *121*, 18326.
[24] L. Liang, X. Li, Y. Sun, Y. Tan, X. Jiao, H. Ju, Z. Qi, J. Zhu, Y. Xie, *Joule* **2018**, *2*, 1004.
[25] A. Kudo, Y. Miseki, *Chem. Soc. Rev.* **2009**, *38*, 253.
[26] X. Chen, S. Shen, L. Guo, S. S. Mao, *Chem. Rev.* **2010**, *110*, 6503.
[27] X. Chen, S. S. Mao, *Chem. Rev.* **2007**, *107*, 2891.
[28] K. M. Lee, C. W. Lai, K. S. Ngai, J. C. Juan, *Water Res.* **2016**, *88*, 428.
[29] P. Ye, X. Liu, J. Iocozzia, Y. Yuan, L. Gu, G. Xu, Z. Lin, *J. Mater. Chem. A* **2017**, *5*, 8493.
[30] J. Hu, A. Liu, H. Jin, D. Ma, D. Yin, P. Ling, S. Wang, Z. Lin, J. Wang, *J. Am. Chem. Soc.* **2015**, *137*, 11004.
[31] Y. Zhao, Y. Zhao, G. I. N. Waterhouse, L. Zheng, X. Cao, F. Teng, L. Z. Wu, C. H. Tung, D. O'Hare, T. Zhang, *Adv. Mater.* **2017**, *29*, 1703828.
[32] R. Shi, Y. Cao, Y. Bao, Y. Zhao, G. I. N. Waterhouse, Z. Fang, L. Z. Wu, C. H. Tung, Y. Yin, T. Zhang, *Adv. Mater.* **2017**, *29*, 1700803.
[33] J. Yan, T. Wang, G. Wu, W. Dai, N. Guan, L. Li, J. Gong, *Adv. Mater.* **2015**, *27*, 1580.
[34] A. Li, X. Chang, Z. Huang, C. Li, Y. Wei, L. Zhang, T. Wang, J. Gong, *Angew. Chem., Int. Ed.* **2016**, *55*, 13734.
[35] L. Li, J. Yan, T. Wang, Z.-J. Zhao, J. Zhang, J. Gong, N. Guan, *Nat. Commun.* **2015**, *6*, 5881.
[36] M.-Q. Yang, B. Weng, Y.-J. Xu, *J. Mater. Chem. A* **2014**, *2*, 1710.
[37] H. Yu, R. Shi, Y. Zhao, T. Bian, Y. Zhao, C. Zhou, G. I. N. Waterhouse, L. Z. Wu, C. H. Tung, T. Zhang, *Adv. Mater.* **2017**, *29*, 1605148.
[38] N. Zhang, C. Han, Y.-J. Xu, J. J. Foley Iv, D. Zhang, J. Codrington, S. K. Gray, Y. Sun, *Nat. Photonics* **2016**, *10*, 473.
[39] J. Li, X. Wu, W. Pan, G. Zhang, H. Chen, *Angew. Chem., Int. Ed.* **2018**, *57*, 491.
[40] Z. Zheng, T. Tachikawa, T. Majima, *J. Am. Chem. Soc.* **2014**, *136*, 6870.
[41] L. Zhu, M. Gao, C. K. N. Peh, G. W. Ho, *Mater. Horiz.* **2018**, *5*, 323.
[42] Z. Gan, X. Wu, M. Meng, X. Zhu, L. Yang, P. K. Chu, *ACS Nano* **2014**, *8*, 9304.
[43] S. Liu, Z.-R. Tang, Y. Sun, J. C. Colmenares, Y.-J. Xu, *Chem. Soc. Rev.* **2015**, *44*, 5053.
[44] B. Ohtani, *Phys. Chem. Chem. Phys.* **2014**, *16*, 1788.
[45] H. L. Tan, R. Amal, Y. H. Ng, *J. Mater. Chem. A* **2017**, *5*, 16498.
[46] J. Park, *J. Ind. Eng. Chem.* **2017**, *51*, 27.
[47] C. Leygraf, M. Hendewerk, G. A. Somorjai, *J. Catal.* **1982**, *78*, 341.
[48] T. Nakahira, M. Grätzel, *Makromol. Chem., Rapid Commun.* **1985**, *6*, 341.
[49] J. Wang, F.-y. Wen, Z.-h. Zhang, X.-D. Zhang, Z.-j. Pan, L. Zhang, L. Wang, L. Xu, P.-l. Kang, P. Zhang, *J. Environ. Sci.* **2005**, *17*, 727.
[50] Z. Li, Y. Dai, X. Ma, Y. Zhu, B. Huang, *Phys. Chem. Chem. Phys.* **2014**, *16*, 3267.
[51] C. Hu, P. Li, W. Zhang, Y. Che, Y. Sun, F. Chi, S. Ran, X. Liu, Y. Lv, *Mater. Res.* **2017**, *20*, 407.
[52] C. Zhang, Z. Du, R. Zhou, P. Xu, X. Dong, Y. Fu, Q. Wang, C. Su, L. Yan, Z. Gu, *RSC Adv.* **2018**, *8*, 3611.
[53] W. Jiang, Z. Wu, X. Yue, S. Yuan, H. Lu, B. Liang, *RSC Adv.* **2015**, *5*, 24064.
[54] Y. Sang, Z. Zhao, M. Zhao, P. Hao, Y. Leng, H. Liu, *Adv. Mater.* **2015**, *27*, 363.
[55] Z. Wu, X. Yuan, H. Wang, Z. Wu, L. Jiang, H. Wang, L. Zhang, Z. Xiao, X. Chen, G. Zeng, *Appl. Catal., B* **2017**, *202*, 104.
[56] M. Zhu, Y. Osakada, S. Kim, M. Fujitsuka, T. Majima, *Appl. Catal., B* **2017**, *217*, 285.
[57] M. Zhu, S. Kim, L. Mao, M. Fujitsuka, J. Zhang, X. Wang, T. Majima, *J. Am. Chem. Soc.* **2017**, *139*, 13234.
[58] M. Zhu, Z. Sun, M. Fujitsuka, T. Majima, *Angew. Chem., Int. Ed.* **2018**, *57*, 2160.
[59] M. Zhu, C. Zhai, M. Fujitsuka, T. Majima, *Appl. Catal., B* **2018**, *221*, 645.
[60] S. Ghosh, N. A. Kouamé, L. Ramos, S. Remita, A. Dazzi, A. Deniset-Besseau, P. Beaunier, F. Goubard, P.-H. Aubert, H. Remita, *Nat. Mater.* **2015**, *14*, 505.
[61] F. Guo, W. Shi, S. Guo, W. Guan, Y. Liu, H. Huang, Y. Liu, Z. Kang, *Appl. Catal., B* **2017**, *210*, 205.
[62] X.-H. Zhang, X.-P. Wang, J. Xiao, S.-Y. Wang, D.-K. Huang, X. Ding, Y.-G. Xiang, H. Chen, *J. Catal.* **2017**, *350*, 64.
[63] Y. Min-Quan, W. Jing, W. Hao, H. G. Wei, *Small* **2018**, *14*, 1703323.
[64] X. Pan, M.-Q. Yang, X. Fu, N. Zhang, Y.-J. Xu, *Nanoscale* **2013**, *5*, 3601.
[65] X. Chen, L. Liu, P. Y. Yu, S. S. Mao, *Science* **2011**, *331*, 746.
[66] Z. Wang, C. Yang, T. Lin, H. Yin, P. Chen, D. Wan, F. Xu, F. Huang, J. Lin, X. Xie, M. Jiang, *Energy Environ. Sci.* **2013**, *6*, 3007.

[67] L. Tian, J. Xu, A. Alnafisah, R. Wang, X. Tan, N. A. Oyler, L. Liu, X. Chen, *Chem. – Eur. J.* **2017**, *23*, 5345.
[68] K. Zhang, L. Wang, J. K. Kim, M. Ma, G. Veerappan, C.-L. Lee, K.-j. Kong, H. Lee, J. H. Park, *Energy Environ. Sci.* **2016**, *9*, 499.
[69] X. Chen, L. Liu, F. Huang, *Chem. Soc. Rev.* **2015**, *44*, 1861.
[70] J. Jiang, X. Tang, S. Zhou, J. Ding, H. Zhou, F. Zhang, D. Zhang, T. Fan, *Green Chem.* **2016**, *18*, 2056.
[71] Y. Li, Z. Wang, T. Xia, H. Ju, K. Zhang, R. Long, Q. Xu, C. Wang, L. Song, J. Zhu, J. Jiang, Y. Xiong, *Adv. Mater.* **2016**, *28*, 6959.
[72] D. Wei, L. Yao, S. Yang, Z. Cui, B. Wei, M. Cao, C. Hu, *ACS Appl. Mater. Interfaces* **2015**, *7*, 20761.
[73] J. Li, N. Wu, *Catal. Sci. Technol.* **2015**, *5*, 1360.
[74] W. Jiang, S. Bai, L. Wang, X. Wang, L. Yang, Y. Li, D. Liu, X. Wang, Z. Li, J. Jiang, Y. Xiong, *Small* **2016**, *12*, 1640.
[75] X. Zhang, T. Peng, S. Song, *J. Mater. Chem. A* **2016**, *4*, 2365.
[76] D. Pei, J. Luan, *Int. J. Photoenergy* **2012**, *2012*, 262831.
[77] K. Takanabe, K. Kamata, X. Wang, M. Antonietti, J. Kubota, K. Domen, *Phys. Chem. Chem. Phys.* **2010**, *12*, 13020.
[78] X. Zhang, L. Yu, C. Zhuang, T. Peng, R. Li, X. Li, *ACS Catal.* **2014**, *4*, 162.
[79] X. Zhang, L. Yu, C. Zhuang, T. Peng, R. Li, X. Li, *RSC Adv.* **2013**, *3*, 14363.
[80] M. Wang, M. Ye, J. Iocozzia, C. Lin, Z. Lin, *Adv. Sci.* **2016**, *3*, 1600024.
[81] C. Han, Q. Quan, H. M. Chen, Y. Sun, Y. J. Xu, *Small* **2017**, *13*, 1602947.
[82] L. Yuan, B. Weng, J. C. Colmenares, Y. Sun, Y. J. Xu, *Small* **2017**, *13*, 1702253.
[83] P. Zhang, T. Wang, J. Gong, *Adv. Mater.* **2015**, *27*, 5328.
[84] O. Elbanna, S. Kim, M. Fujitsuka, T. Majima, *Nano Energy* **2017**, *35*, 1.
[85] J.-H. Wang, M. Chen, Z.-J. Luo, L. Ma, Y.-F. Zhang, K. Chen, L. Zhou, Q.-Q. Wang, *J. Phys. Chem. C* **2016**, *120*, 14805.
[86] R. Yan, M. Chen, H. Zhou, T. Liu, X. Tang, K. Zhang, H. Zhu, J. Ye, D. Zhang, T. Fan, *Sci. Rep.* **2016**, *6*, 20001.
[87] K.-H. Chen, Y.-C. Pu, K.-D. Chang, Y.-F. Liang, C.-M. Liu, J.-W. Yeh, H.-C. Shih, Y.-J. Hsu, *J. Phys. Chem. C* **2012**, *116*, 19039.
[88] P. Zhang, T. Song, T. Wang, H. Zeng, *Appl. Catal., B* **2018**, *225*, 172.
[89] P. Zhang, T. Song, T. Wang, H. Zeng, *J. Mater. Chem. A* **2017**, *5*, 22772.
[90] B. Weng, K.-Q. Lu, Z. Tang, H. M. Chen, Y.-J. Xu, *Nat. Commun.* **2018**, *9*, 1543.
[91] X. Li, F. Zhang, D. Zhao, *Nano Today* **2013**, *8*, 643.
[92] W. Yang, X. Li, D. Chi, H. Zhang, X. Liu, *Nanotechnol.* **2014**, *25*, 482001.
[93] W. Fan, H. Bai, W. Shi, *CrystEngComm* **2014**, *16*, 3059.
[94] Y. Zhang, Z. Hong, *Nanoscale* **2013**, *5*, 8930.
[95] W. Wang, Y. Li, Z. Kang, F. Wang, J. C. Yu, *Appl. Catal., B* **2016**, *182*, 184.
[96] W. Wang, M. Ding, C. Lu, Y. Ni, Z. Xu, *Appl. Catal., B* **2014**, *144*, 379.
[97] Y. Tang, W. Di, X. Zhai, R. Yang, W. Qin, *ACS Catal.* **2013**, *3*, 405.
[98] L. Bai, W. Jiang, C. Gao, S. Zhong, L. Zhao, Z. Li, S. Bai, *Nanoscale* **2016**, *8*, 19014.
[99] S. Huang, Y. Feng, L. Han, W. Fan, X. Zhao, Z. Lou, Z. Qi, B. Yu, N. Zhu, *RSC Adv.* **2014**, *4*, 61679.
[100] Y. Chen, S. Mishra, G. Ledoux, E. Jeanneau, M. Daniel, J. Zhang, S. Daniele, *Chem. – Asian J.* **2014**, *9*, 2415.
[101] F. Zhang, W. N. Wang, H. P. Cong, L. B. Luo, Z. B. Zha, H. S. Qian, *Part. Part. Syst. Charact.* **2017**, *34*, 1600222.
[102] S. Huang, N. Zhu, Z. Lou, L. Gu, C. Miao, H. Yuan, A. Shan, *Nanoscale* **2014**, *6*, 1362.
[103] W. Feng, L. Zhang, Y. Zhang, Y. Yang, Z. Fang, B. Wang, S. Zhang, P. Liu, *J. Mater. Chem. A* **2017**, *5*, 10311.
[104] Z. Xu, M. Quintanilla, F. Vetrone, A. O. Govorov, M. Chaker, D. Ma, *Adv. Funct. Mater.* **2015**, *25*, 2950.
[105] H. Yu, R. Shi, Y. Zhao, G. I. N. Waterhouse, L. Z. Wu, C. H. Tung, T. Zhang, *Adv. Mater.* **2016**, *28*, 9454.
[106] K. A. S. Fernando, S. Sahu, Y. Liu, W. K. Lewis, E. A. Guliants, A. Jafariyan, P. Wang, C. E. Bunker, Y.-P. Sun, *ACS Appl. Mater. Interfaces* **2015**, *7*, 8363.
[107] S. Zhu, Y. Song, X. Zhao, J. Shao, J. Zhang, B. Yang, *Nano Res.* **2015**, *8*, 355.
[108] M. Hassan, V. G. Gomes, A. Dehghani, S. M. Ardekani, *Nano Res.* **2018**, *11*, 1.
[109] H. Li, R. Liu, Y. Liu, H. Huang, H. Yu, H. Ming, S. Lian, S.-T. Lee, Z. Kang, *J. Mater. Chem.* **2012**, *22*, 17470.
[110] Y. Hao, X. Dong, S. Zhai, X. Wang, H. Ma, X. Zhang, *Chem. Commun.* **2016**, *52*, 6525.
[111] B. Liu, X. Zhao, C. Terashima, A. Fujishima, K. Nakata, *Phys. Chem. Chem. Phys.* **2014**, *16*, 8751.
[112] E. Nurlaela, T. Shinagawa, M. Qureshi, D. S. Dhawale, K. Takanabe, *ACS Catal.* **2016**, *6*, 1713.
[113] S. I. Nikitenko, T. Chave, C. Cau, H.-P. Brau, V. Flaud, *ACS Catal.* **2015**, *5*, 4790.
[114] Z. Zhang, W. Wang, E. Gao, S. Sun, L. Zhang, *J. Phys. Chem. C* **2012**, *116*, 25898.
[115] G. Ni, N. Miljkovic, H. Ghasemi, X. Huang, S. V. Boriskina, C.-T. Lin, J. Wang, Y. Xu, M. M. Rahman, T. Zhang, G. Chen, *Nano Energy* **2015**, *17*, 290.
[116] X. Gao, H. Ren, J. Zhou, R. Du, C. Yin, R. Liu, H. Peng, L. Tong, Z. Liu, J. Zhang, *Chem. Mater.* **2017**, *29*, 5777.
[117] M. Gao, L. Zhu, W. L. Ong, J. Wang, G. W. Ho, *Catal. Sci. Technol.* **2015**, *5*, 4703.
[118] N. Zhang, M.-Q. Yang, S. Liu, Y. Sun, Y.-J. Xu, *Chem. Rev.* **2015**, *115*, 10307.
[119] M.-Q. Yang, C. Han, N. Zhang, Y.-J. Xu, *Nanoscale* **2015**, *7*, 18062.
[120] X. Pan, M.-Q. Yang, Z.-R. Tang, Y.-J. Xu, *J. Phys. Chem. C* **2014**, *118*, 27325.
[121] K.-Q. Lu, L. Yuan, X. Xin, Y.-J. Xu, *Appl. Catal., B* **2018**, *226*, 16.
[122] G. M. Neelgund, A. Oki, *Mater. Chem. Front.* **2018**, *2*, 64.
[123] Y. Bai, P. Yang, P. Wang, H. Xie, H. Dang, L. Ye, *J. CO2 Util.* **2018**, *23*, 51.
[124] J. Hu, H. Wang, F. Dong, Z. Wu, *Appl. Catal., B* **2017**, *204*, 584.
[125] J. Fang, Z. Chen, Q. Zheng, D. Li, *Catal. Sci. Technol.* **2017**, *7*, 3303.
[126] M. Zeng, Y. Li, M. Mao, J. Bai, L. Ren, X. Zhao, *ACS Catal.* **2015**, *5*, 3278.
[127] H. Liu, Y. Li, Y. Yang, M. Mao, M. Zeng, L. Lan, L. Yun, X. Zhao, *J. Mater. Chem. A* **2016**, *4*, 9890.
[128] K. Sugawa, N. Tsunenari, H. Takeda, S. Fujiwara, T. Akiyama, J. Honda, S. Igari, W. Inoue, K. Tokuda, N. Takeshima, Y. Watanuki, S. Tsukahara, K. Takase, T. Umegaki, Y. Kojima, N. Nishimiya, N. Fukuda, Y. Kusaka, H. Ushijima, J. Otsuki, *Langmuir* **2017**, *33*, 5685.
[129] G. Li, C. Guo, M. Yan, S. Liu, *Appl. Catal., B* **2016**, *183*, 142.
[130] H. Che, C. Liu, W. Hu, H. Hu, J. Li, J. Dou, W. Shi, C. Li, H. Dong, *Catal. Sci. Technol.* **2018**, *8*, 622.
[131] X. Hu, C. Hu, R. Wang, *Appl. Catal., B* **2015**, *176–177*, 637.
[132] X. Wu, S. Yin, Q. Dong, B. Liu, Y. Wang, T. Sekino, S. W. Lee, T. Sato, *Sci. Rep.* **2013**, *3*, 2918.
[133] X. Wu, S. Yin, Q. Dong, T. Sato, *Appl. Catal., B* **2014**, *156–157*, 257.
[134] G. Cui, W. Wang, M. Ma, J. Xie, X. Shi, N. Deng, J. Xin, B. Tang, *Nano Lett.* **2015**, *15*, 7199.
[135] Y. L. Wang, T. Nie, Y. H. Li, X. L. Wang, L. R. Zheng, A. P. Chen, X. Q. Gong, H. G. Yang, *Angew. Chem., Int. Ed.* **2017**, *56*, 7430.
[136] L. Ye, H. Wang, X. Jin, Y. Su, D. Wang, H. Xie, X. Liu, X. Liu, *Sol. Energy Mater. Sol. Cells* **2016**, *144*, 732.
[137] F. Wang, Y. Huang, Z. Chai, M. Zeng, Q. Li, Y. Wang, D. Xu, *Chem. Sci.* **2016**, *7*, 6887.

[138] S. Linic, P. Christopher, D. B. Ingram, *Nat. Mater.* **2011**, *10*, 911.
[139] S. Sarina, H. Y. Zhu, Q. Xiao, E. Jaatinen, J. Jia, Y. Huang, Z. Zheng, H. Wu, *Angew. Chem., Int. Ed.* **2014**, *53*, 2935.
[140] N. A. M. Barakat, M. A. Kanjwal, I. S. Chronakis, H. Y. Kim, *J. Mol. Catal. A: Chem.* **2013**, *366*, 333.
[141] J. Méndez-Ramos, J. C. Ruiz-Morales, P. Acosta-Mora, J. del-Castillo, A. C. Yanes, *J. Power Sources* **2013**, *238*, 313.
[142] M. Yoshimizu, R. Kobayashi, M. Saegusa, T. Takashima, H. Funakubo, K. Akiyama, Y. Matsumoto, H. Irie, *Chem. Commun.* **2015**, *51*, 2818.
[143] Y. Takimoto, T. Kitta, H. Irie, *Int. J. Hydrogen Energy* **2012**, *37*, 134.
[144] H. Wen, H. Li, S. He, F. Chen, E. Ding, S. Liu, B. Wang, Y. Peng, *Nanoscale* **2018**, *10*, 2380.
[145] A. Gannoruwa, K. Niroshan, O. A. Ileperuma, J. Bandara, *Int. J. Hydrogen Energy* **2014**, *39*, 15411.
[146] S. L. Wang, Y. L. Mak, S. Wang, J. Chai, F. Pan, M. L. Foo, W. Chen, K. Wu, G. Q. Xu, *Langmuir* **2016**, *32*, 13046.
[147] Y. Zhou, P. Liu, F. Jiang, J. Tian, H. Cui, J. Yang, *J. Colloid Interface Sci.* **2017**, *498*, 442.
[148] K. Yaemsunthorn, T. Thongtem, S. Thongtem, C. Randorn, *Mater. Sci. Semicond. Process.* **2017**, *68*, 53.
[149] W. Jiang, X. Wang, Z. Wu, X. Yue, S. Yuan, H. Lu, B. Liang, *Ind. Eng. Chem. Res.* **2015**, *54*, 832.
[150] W. Gao, W. Liu, Y. Leng, X. Wang, X. Wang, B. Hu, D. Yu, Y. Sang, H. Liu, *Appl. Catal., B* **2015**, *176–177*, 83.
[151] Y. Li, T. Li, J. Tian, X. Wang, H. Cui, *Part. Part. Syst. Charact.* **2017**, *34*, 1700127.
[152] X. Liu, X. Wu, J. Li, L. Liu, Y. Ma, *Catal. Commun.* **2017**, *91*, 21.
[153] N. Wei, H. Cui, Q. Song, L. Zhang, X. Song, K. Wang, Y. Zhang, J. Li, J. Wen, J. Tian, *Appl. Catal., B* **2016**, *198*, 83.
[154] X. Hu, Y. Li, J. Tian, H. Yang, H. Cui, *J. Ind. Eng. Chem.* **2017**, *45*, 189.
[155] Y. Li, Y. Xue, J. Tian, X. Song, X. Zhang, X. Wang, H. Cui, *Sol. Energy Mater. Sol. Cells* **2017**, *168*, 100.
[156] H. Yang, J. Tian, T. Li, H. Cui, *Catal. Commun.* **2016**, *87*, 82.
[157] Y. Chen, G. Zhu, M. Hojamberdiev, J. Gao, R. Zhu, C. Wang, X. Wei, P. Liu, *J. Hazard. Mater.* **2018**, *344*, 42.
[158] K. M. S. D. B. Kulathunga, A. Gannoruwa, J. Bandara, *Catal. Commun.* **2016**, *86*, 9.
[159] H. Chen, W. Liu, Z. Qin, *Catal. Sci. Technol.* **2017**, *7*, 2236.
[160] L. Zhang, W. Wang, S. Sun, D. Jiang, *Appl. Catal., B* **2015**, *168–169*, 9.
[161] T. Liu, B. Liu, L. Yang, X. Ma, H. Li, S. Yin, T. Sato, T. Sekino, Y. Wang, *Appl. Catal., B* **2017**, *204*, 593.
[162] J. Li, W. Li, X. Li, Y. Li, H. Bai, M. Li, G. Xi, *RSC Adv.* **2017**, *7*, 23846.
[163] H. Zhou, S. Xu, D. Zhang, S. Chen, J. Deng, *Nanoscale* **2017**, *9*, 3196.
[164] H. Chen, W. Liu, B. Hu, Z. Qin, H. Liu, *Nanoscale* **2017**, *9*, 18940.
[165] L. Wang, Y. Wan, Y. Ding, Y. Niu, Y. Xiong, X. Wu, H. Xu, *Nanoscale* **2017**, *9*, 4090.
[166] Y. Guo, S. Song, Y. Zheng, R. Li, T. Peng, *Dalton Trans.* **2016**, *45*, 14071.
[167] Y. Sun, X.-F. Wang, G. Chen, C.-H. Zhan, O. Kitao, H. Tamiaki, S.-i. Sasaki, *Int. J. Hydrogen Energy* **2017**, *42*, 15731.
[168] Z. Zhang, W. Wang, L. Zhang, *Dalton Trans.* **2013**, *42*, 4579.
[169] M. Zhu, X. Cai, M. Fujitsuka, J. Zhang, T. Majima, *Angew. Chem., Int. Ed.* **2017**, *56*, 2064.
[170] X. Cai, M. Zhu, O. A. Elbanna, M. Fujitsuka, S. Kim, L. Mao, J. Zhang, T. Majima, *ACS Catal.* **2018**, *8*, 122.
[171] H. Ji, L. Lyu, L. Zhang, X. An, C. Hu, *Appl. Catal., B* **2016**, *199*, 230.
[172] Y. Deng, L. Tang, C. Feng, G. Zeng, J. Wang, Y. Zhou, Y. Liu, B. Peng, H. Feng, *J. Hazard. Mater.* **2018**, *344*, 758.
[173] N. Zhang, M. Li, C. F. Tan, C. K. Nuo Peh, T. C. Sum, G. W. Ho, *J. Mater. Chem. A* **2017**, *5*, 21570.
[174] W. Shi, H. Lv, S. Yuan, H. Huang, Y. Liu, Z. Kang, *Sep. Purif. Technol.* **2017**, *174*, 75.
[175] S. Ullah, C. Hazra, E. P. Ferreira-Neto, T. C. Silva, U. P. Rodrigues-Filho, S. J. L. Ribeiro, *CrystEngComm* **2017**, *19*, 3465.
[176] W. Su, M. Zheng, L. Li, K. Wang, R. Qiao, Y. Zhong, Y. Hu, Z. Li, *J. Mater. Chem. A* **2014**, *2*, 13486.
[177] F. Zhang, C. L. Zhang, H. Y. Peng, H. P. Cong, H. S. Qian, *Part. Part. Syst. Charact.* **2016**, *33*, 248.
[178] Y. Gao, C. Shi, J. Feng, G. Zhao, H. Yu, Y. Bi, F. Ding, Y. Sun, Z. Xu, *RSC Adv.* **2017**, *7*, 54555.
[179] S. Huang, Z. Lou, A. Shan, N. Zhu, K. Feng, H. Yuan, *J. Mater. Chem. A* **2014**, *2*, 16165.
[180] E. Cheng, W. Yin, S. Bai, R. Qiao, Y. Zhong, Z. Li, *Mater. Lett.* **2015**, *146*, 87.
[181] S. Huang, L. Gu, C. Miao, Z. Lou, N. Zhu, H. Yuan, A. Shan, *J. Mater. Chem. A* **2013**, *1*, 7874.
[182] S. Ganguli, C. Hazra, M. Chatti, T. Samanta, V. Mahalingam, *Langmuir* **2016**, *32*, 247.
[183] R. Balaji, S. Kumar, K. L. Reddy, V. Sharma, K. Bhattacharyya, V. Krishnan, *J. Alloys Compd.* **2017**, *724*, 481.
[184] D. Yin, L. Zhang, X. Cao, Z. Chen, J. Tang, Y. Liu, T. Zhang, M. Wu, *Dalton Trans.* **2016**, *45*, 1467.
[185] Y. Lv, L. Yue, Q. Li, B. Shao, S. Zhao, H. Wang, S. Wu, Z. Wang, *Dalton Trans.* **2018**, *47*, 1666.
[186] S. Huang, H. Wang, N. Zhu, Z. Lou, L. Li, A. Shan, H. Yuan, *Appl. Catal., B* **2016**, *181*, 456.
[187] Z. Wu, X. Yuan, G. Zeng, L. Jiang, H. Zhong, Y. Xie, H. Wang, X. Chen, H. Wang, *Appl. Catal., B* **2018**, *225*, 8.
[188] S. Huang, S. Guo, Q. Wang, N. Zhu, Z. Lou, L. Li, A. Shan, H. Yuan, *ACS Appl. Mater. Interfaces* **2015**, *7*, 20170.
[189] W. Wang, W. Huang, Y. Ni, C. Lu, Z. Xu, *ACS Appl. Mater. Interfaces* **2014**, *6*, 340.
[190] J. Zhang, Y. Huang, L. Jin, F. Rosei, F. Vetrone, J. P. Claverie, *ACS Appl. Mater. Interfaces* **2017**, *9*, 8142.
[191] Y. Yang, W. Que, X. Zhang, X. Yin, Y. Xing, M. Que, H. Zhao, Y. Du, *Appl. Catal., B* **2017**, *200*, 402.
[192] J. Qin, H. Zeng, *Appl. Catal., B* **2017**, *209*, 161.
[193] Y. Deng, L. Tang, C. Feng, G. Zeng, J. Wang, Y. Lu, Y. Liu, J. Yu, S. Chen, Y. Zhou, *ACS Appl. Mater. Interfaces* **2017**, *9*, 42816.
[194] Z. Zhang, T. Zheng, J. Xu, H. Zeng, N. Zhang, *J. Photochem. Photobiol. A* **2017**, *346*, 24.
[195] J. Zhang, Y. Ma, Y. Du, H. Jiang, D. Zhou, S. Dong, *Appl. Catal., B* **2017**, *209*, 253.
[196] Y. Guo, P. Yao, D. Zhu, C. Gu, *J. Mater. Chem. A* **2015**, *3*, 13189.
[197] J. Tian, Y. Leng, Z. Zhao, Y. Xia, Y. Sang, P. Hao, J. Zhan, M. Li, H. Liu, *Nano Energy* **2015**, *11*, 419.
[198] J. Chen, H. Che, K. Huang, C. Liu, W. Shi, *Appl. Catal., B* **2016**, *192*, 134.
[199] M. C. Ortega-Liebana, J. L. Hueso, A. Larrea, V. Sebastian, J. Santamaria, *Chem. Commun.* **2015**, *51*, 16625.
[200] X. Liu, L. Ye, Z. Ma, C. Han, L. Wang, Z. Jia, F. Su, H. Xie, *Catal. Commun.* **2017**, *102*, 13.